

Molecular Composition Analysis of Distant Targets

NIAC Phase I, Final Report: 15-NIAC16A-0145

24 February 2017



Gary B. Hughes

California Polytechnic State University

Statistics Department, 25-107G

1 Grand Avenue

San Luis Obispo, CA 93407-0405

gbhughes@calpoly.edu

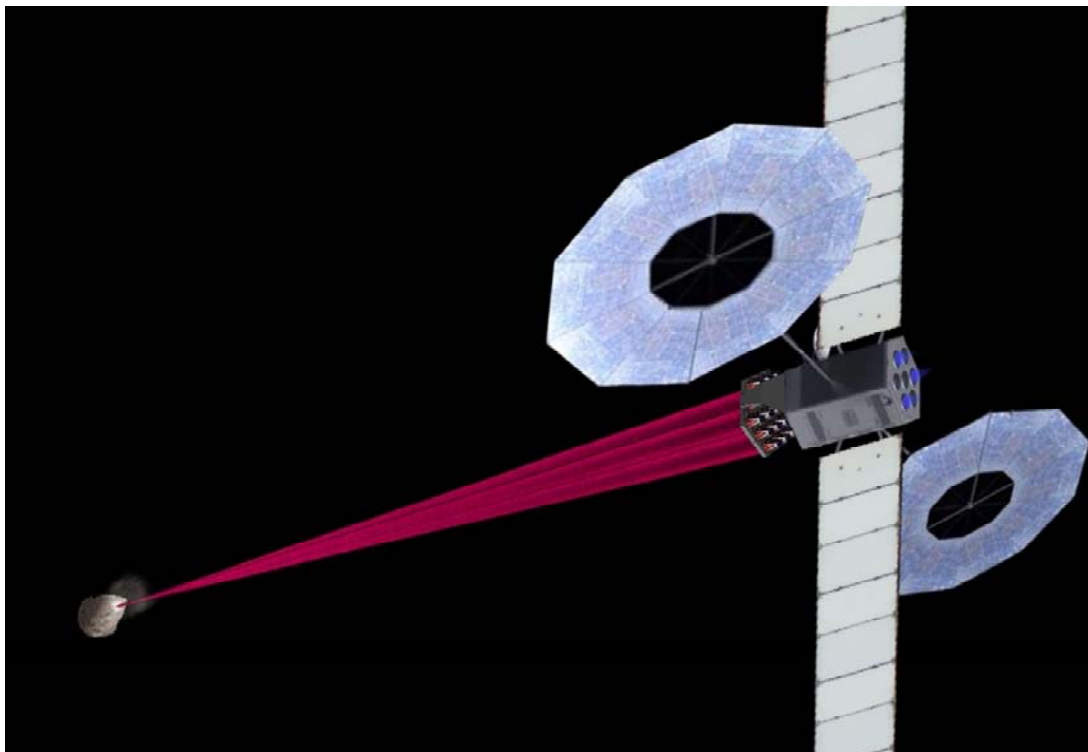
Philip Lubin

University of California, Santa Barbara

Physics Department, Broida 2015C

Santa Barbara, CA 93106-9530

lubin@deepspace.ucsb.edu



Contents

1. INTRODUCTION	4
1.1 Executive Summary	4
1.2 Motivation for Developing Remote Composition Analysis Capability	4
1.2.1 Support for Investigations Involving Mechanisms of Solar System Formation	5
1.2.2 Planetary Defense from Threatening Asteroids and Comets	6
1.2.3 Quest for Water, Economic and Mission Resources, and Organic Materials	7
1.2.4 Linking Asteroid Classification and Composition	7
2. DETAILED DESCRIPTION AND BENEFITS OF THE CONCEPT	8
2.1 System Concept for Molecular Composition Analysis from a Distance	8
2.2 Comparisons to Existing Methods of Remote Composition Analysis	9
2.2.1 Laser-Induced Breakdown Spectroscopy (LIBS)	9
2.2.2 Laser-Induced Thermal Emission (LITE) Spectroscopy	9
2.2.3 Remote Laser Evaporative Molecular Absorption (R-LEMA) Spectroscopy	10
3. NASA MISSION APPLICATIONS	10
3.1 Utility for Asteroid Redirect Mission (ARM)	10
3.2 Mission Design Architecture	11
3.2.1 Spacecraft Design Principle	11
3.2.2 Photovoltaic (PV) Panels	11
3.2.3 Laser Array Design	12
3.2.4 Secondary Optical Configuration of the Laser Array	13
3.2.5 Spacecraft Thermal Management	14
3.2.6 Potential Launch Vehicles	15
3.3 Extended Mission Capability of R-LEMA System	16
4. CONCEPT EVALUATION APPROACH	17
4.1 End-to-End System Model	17
4.2 Evaluation of the Sensor System Concept	18
5. TECHNICAL DETAILS SUPPORTING CONCEPT FEASIBILITY	18
5.1 Laser Optical Propagation Model	18
5.1.1 Laser Phased Array Concept	18
5.1.2 Far-Field Intensity Model of Phased Array Beams	19
5.1.3 Effects of Phase Perturbations in the Optical Model	20
5.1.4 Optical Simulation Results	21
5.1.5 Simulations with Time-Varying Perturbations	22
5.2 Target Thermal Model	23
5.2.1 Energy Conservation Principles During Laser Bombardment of Target	24
5.2.2 1D Energetics Simulations	26
5.2.3 2D Analytic Calculations	26
5.2.4 3D Numeric Calculations and Simulations	27
5.2.5 Comparison of Results among Thermal Simulations	29
5.2.6 Asteroid Thermal Properties	29
5.2.7 Effects of Rotation on Substrate Thermal Heating	31

5.3	Evaporation of Target Material and Resulting Plume Density	34
5.4	Molecular Absorption of Radiation from the Heated Spot in the Ejected Plume	38
5.5	Spectroscopy by Observation of Radiated Energy through the Ejected Plume	39
5.6	Simulations of Absorption Spectra	43
5.7	Analysis of Extended Mission Capability	44
5.7.1	Orbital Deflection of Threatening Asteroids	44
5.7.2	Active Illumination for Threatening Asteroid Discovery	47
5.7.3	Laser-Beamed Spacecraft Propulsion, Power and Communications.....	48
6.	TECHNICAL GOALS AND CHALLENGES BEYOND PHASE I.....	49
6.1	Experimental Approach for Elevating System Readiness.....	49
7.	CONCLUSIONS	52
8.	ACKNOWLEDGEMENTS.....	52
9.	REFERENCES	53

1. INTRODUCTION

1.1 Executive Summary

This document is the Final Report for NASA Innovative Advanced Concepts (NIAC) Phase I Grant 15-NIAC16A-0145, titled “Molecular Composition Analysis of Distant Targets”. The research was focused on developing a system concept for probing the molecular composition of cold solar system targets, such as Asteroids, Comets, Planets and Moons from a distant vantage, for example from a spacecraft that is orbiting the target (Hughes *et al.*, 2015). The orbiting spacecraft is equipped with a high-power laser, which is run by electricity from photovoltaic panels. The laser is directed at a spot on the target. Materials on the surface of the target are heated by the laser beam, and begin to melt and then evaporate, forming a plume of asteroid molecules in front of the heated spot. The heated spot glows, producing blackbody illumination that is visible from the spacecraft, via a path through the evaporated plume. As the blackbody radiation from the heated spot passes through the plume of evaporated material, molecules in the plume absorb radiation in a manner that is specific to the rotational and vibrational characteristics of the specific molecules. A spectrometer aboard the spacecraft is used to observe absorption lines in the blackbody signal. The pattern of absorption can be used to estimate the molecular composition of materials in the plume, which originated on the target. Focusing on a single spot produces a borehole, and shallow subsurface profiling of the target’s bulk composition is possible.

At the beginning of the Phase I research, the estimated Technology Readiness Level (TRL) of the system was TRL-1. During the Phase I research, an end-to-end theoretical model of the sensor system was developed from first principles. The model includes laser energy and optical propagation, target heating, melting and evaporation of target material, plume density, thermal radiation from the heated spot, molecular cross section of likely asteroid materials, and estimation of the absorption profile at a distant spectrometer. Results obtained by executing simulations based on the model provide compelling evidence that the concept of remote laser evaporative molecular absorption spectroscopy is feasible. In this document, technical details of the model are presented, and results of simulations are described that indicate the utility of the proposed sensor system. Additionally, an asteroid rendezvous mission is analyzed, with a survey of system requirements to accomplish molecular composition analysis of the asteroid. Based on positive theoretical results obtained during Phase I, the estimated TRL of the system is now TRL-2. This document also describes potential future research and experimentation that could push the system to TRL-4 within 2 years. Steps required for construction of a laboratory prototype are described. An experiment to test predictions of the theory is described, based on the laboratory prototype setup.

1.2 Motivation for Developing Remote Composition Analysis Capability

Why is it important to study the molecular composition of cold solar system targets? Such research is motivated by diverse interests. Asteroids and comets represent primordial material from the beginning of the solar system, and understanding their composition contributes invaluable information to studies of solar system formation. The search for organic material on asteroids and comets can spur insight into the origins of life on Earth. More practical motivations have also been spurred by recent technological advances. Interest is growing in the potential benefits of economic resources of asteroids, including metals and other ores. Asteroids also harbor resources that could benefit deep-space exploration, as replenishment outposts for longer journeys.

1.2.1 Support for Investigations Involving Mechanisms of Solar System Formation

Asteroids and comets are icy and rocky remnants of the formation of our solar system. Astronomical surveillance activities have identified more than 600 000 asteroids, and discovery continues at a rapidly increasing pace. Most of these objects remain in stable orbits around the Sun, within a ‘main belt’ of objects moving in stable orbits between Mars and Jupiter; a schematic distribution of asteroids in the solar system is shown in Figure 1-1. Main belt asteroids can sometimes be perturbed from their stable orbits, mainly through the process of Yarkovsky thermal drag (Morbidelli, 2005), but occasionally through interaction with other asteroids or planets. Orbital perturbations can deflect asteroids toward the inner planets, including into paths that cross Earth’s orbit. Asteroids that approach or cross Earth’s orbit are deemed Near Earth Asteroids (NEAs). A slightly larger class, including asteroids and comets, is referred to as Near Earth Objects (NEOs). NEOs are best characterized as transient objects, *i.e.*, the average lifetime of NEOs is relatively short, perhaps only a few million years (Gladman *et al.*, 1997). Objects that linger in the inner solar system are eventually removed or destroyed, either by direct collision with a planet or the Sun, or by ejection from the solar system via orbit alteration. The comet ISON appeared to disintegrate on 28 November 2013 when its orbit passed too close to the Sun.

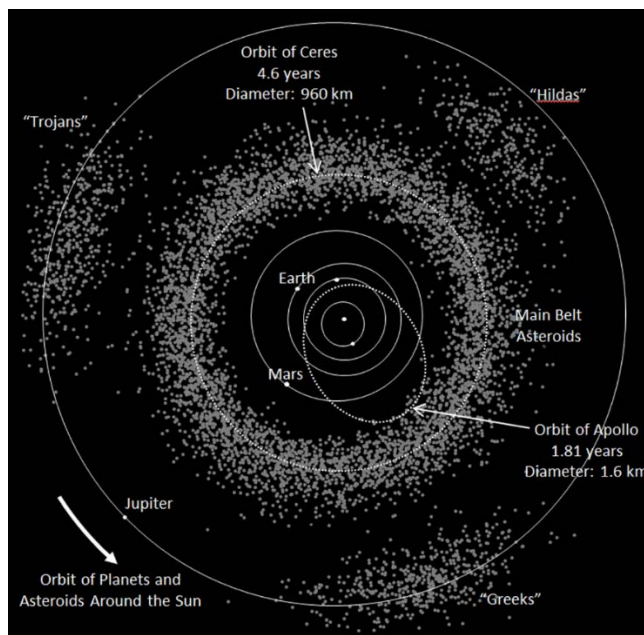


Figure 1-1: This diagram is a schematic representation of main-belt asteroid orbits. The view is from a point above the ecliptic plane, looking downward onto the ecliptic plane such that the sun is in the center. The scale of the diagram is such that the orbit of Jupiter is a circular feature that grazes the edges of the diagram. The orbits of Mars, Earth, Venus and Mercury are also shown, and all orbits proceed counter clockwise as viewed from above. Main belt asteroids form a large group of objects that orbit the Sun between Mars and Jupiter. Ceres, with a mean diameter of 952 km, is the largest known asteroid, and is ensconced in a main-belt orbit. Main-belt objects can be deflected into the inner solar system, posing a threat to Earth. The orbit of Apollo is shown, passing from the inner main belt all the way inside the orbit of Venus.

Investigation of the composition of comets and asteroids can provide insight into the formation of the solar system. The solar system formed from an immense cloud of gas and dust (the solar nebula), which condensed due to gravitational attraction. Remnants of the original nebula are not available on Earth, at least in a form close to their original condition in the solar nebula. But, some asteroids and comets contain partially altered nebular materials. Examining the composition of these primordial objects provides insight into the composition of the solar nebula, and also into the conditions of the early solar system that led to the current mineral forms exhibited in the ancient materials. Direct interrogation of the molecular composition of asteroids and comets is a complex and expensive proposition. A system capable of remote interrogation would represent a compelling potential benefit for solar system exploration by establishing the capability to directly interrogate the bulk composition of objects from a distant vantage.

1.2.2 Planetary Defense from Threatening Asteroids and Comets

Dinosaurs roamed the Earth for almost two hundred million years. They were likely wiped out in a geologic instant when a ~10-kilometer-wide asteroid struck Earth around 66 million years ago (Alvarez *et al.*, 1980). The suspected crater, ~180 kilometers in diameter, is discernible near the Yucatán Peninsula, México (Hildebrand *et al.*, 1991), providing an ominous reminder of the power unleashed by the asteroid impact. Fast forward to 15 February 2013: an asteroid that was ~20 meters wide barreled through the atmosphere, and struck Earth near Chelyabinsk, Russia (Popova *et al.*, 2014). Fortuitously, the impact occurred in an area with numerous dash-cams and video surveillance systems, and the spectacular fireball was recorded from hundreds of different vantages. The airburst over Chelyabinsk released energy equivalent to ~570 kilotons of TNT, which is nearly 50 times more powerful than the nuclear bomb that was detonated in Hiroshima, Japan in 1945 (Glasstone and Dolan, 1977). The Chelyabinsk impact resulted in over 1200 injuries, with property damage in the range US\$33-50 million, all caused by an asteroid that was not previously observed.

The presumed fate of the dinosaurs, and the extraordinary event in Chelyabinsk, serve as stark reminders that the Earth is relentlessly being pelted by space rocks, small and large. When can we expect another event like Chelyabinsk? Is another dinosaur killer ever coming our way, or perhaps anytime soon? Where do asteroids come from in the first place? How many are there? What are asteroids made of? Can they reveal anything about the history of Earth, or about the ‘place’ (in an existential sense) that Earth occupies in the solar system? Modern Research efforts around the globe are chipping away at the enigma of asteroids.

Main belt asteroids that perturbed from their stable main-belt orbits can be diverted toward the inner planets, including into paths that approach or cross Earth’s orbit; such objects are deemed Near Earth Asteroids (NEAs). A slightly larger class, including asteroids and comets, is referred to as Near Earth Objects (NEOs). NEOs are best characterized as transient objects, *i.e.*, the average lifetime of NEOs is relatively short, perhaps only a few million years (Gladman *et al.*, 1977). Objects that linger in the inner solar system are eventually removed or destroyed, either by direct collision with a planet or the Sun, or by ejection from the solar system via orbit alteration. The comet ISON appeared to disintegrate on 28 November 2013 when its orbit passed too close to the Sun. The Chelyabinsk impactor originated in the main belt.

In order to evaluate the threat posed to Earth and society, continued efforts to discover more objects in the unknown population are imperative. NASA recently formed the Planetary Defense Coordination Office (PDCO), dedicated to finding and characterizing asteroids and

comets that pass near Earth's orbit around the sun. In addition to discovery and orbit determination, it is also crucial to understand the physical properties of bolides, particularly size and composition.

1.2.3 Quest for Water, Economic and Mission Resources, and Organic Materials

Perhaps ironically, investigating asteroid composition could also prove useful to efforts aimed at exploiting asteroids for their mineral resources. The determination of the composition of asteroids and other targets supports potential future resource extraction by pre-determining the materials in the target before mining missions are deployed. Resource extraction in the solar system will become increasingly important and remote molecular composition analysis will likely play an important role in surveillance of potential targets. In operational scenarios, interrogation of asteroid molecular composition could target species that might be important for mineral resources (Klossek *et al.*, 2016; Müller *et al.*, 2016; Jakhu and Buzdugan, 2008), or for in-situ resource utilization for deep space missions (Sanchez and McInnes, 2012). For example, water or methane could be utilized as fuel on outposts along the path to Mars.

1.2.4 Linking Asteroid Classification and Composition

Current knowledge of asteroid composition comes mainly from observations of reflected light over optical and near-infrared wavelengths (DeMeo *et al.*, 2009). Asteroids are classified within a taxonomy based on spectral characteristics of the reflected light, which derives primarily from properties of surface material. Occasionally, bulk composition can be studied directly when meteorites such as the Chelyabinsk impactor are recovered, providing additional insight about composition of objects in the spectral class to which the parent asteroid belonged. For many asteroids, light reflected from the surface can only divulge information about surface material, which is often a fine dust coating ('regolith') that may or may not be derived from, or representative of, the asteroid's bulk composition. Regolith may be altered material from the asteroid, or it may be derived from accumulation of debris from other sources, or some combination thereof.

Direct sampling of asteroid and comet material has been limited to a few missions. The Hayabusa mission by the Japanese Aerospace Exploration Agency (JAXA) collected and returned samples from the surface of asteroid 25143 Itokawa (Yoshikawa *et al.*, 2006). The sample consisted of approximately 1 g of particles in the size range 10-100 μm , mainly from regolith. NASA's Deep Impact mission to comet 9P/Tempel sought to excavate sub-surface material by sending an impactor to the surface (A'Hearn *et al.*, 2005). Emission spectra of the heated ejecta were obtained, and analyzed for composition (Lisse *et al.*, 2006). NASA's Stardust mission navigated through the coma of comet 81P/Wild, and returned samples to Earth (Brownlee *et al.*, 2006). The European Space Agency's (ESA) Philae lander of the Rosetta mission analyzed surface samples of comet 67P/Churyumov-Gerasimenko, sending data recorded *in situ* on the comet back to Earth (Glassmeier *et al.*, 2007). NASA's Osiris-Rex mission, with a launch window beginning on 08 September 2016, aims to rendezvous with asteroid 101955 Bennu, perform a 'touch-and-go' maneuver, and then return samples of surface material to Earth (Berry *et al.*, 2013).

Missions to directly assess asteroid composition are notable for their ingenuity and tenacity in the face of very difficult mission scenarios. Due to overall mission complexity, sample-return or landing/*in situ* measurement missions are likely to be limited in scope and number for the foreseeable future. It would be very beneficial to be able to make direct measurements of the bulk composition of asteroids from a distance.

2. DETAILED DESCRIPTION AND BENEFITS OF THE CONCEPT

2.1 System Concept for Molecular Composition Analysis from a Distance

The NASA Innovative Advanced Research (NIAC) project “Molecular Composition Analysis of Distant Targets” proposes a method for probing the molecular composition of cold solar system targets (asteroids, comets, planets, moons) from a distant vantage, such as from a spacecraft orbiting the object. The spacecraft includes a solar-powered laser array. A directed energy beam from the laser is focused on the target. With target flux in the range of $\sim 10 \text{ MW/m}^2$, the spot temperature rises rapidly, to $\sim 2500 \text{ K}$ for rocky targets, and melting and evaporation of surface materials on the target occurs. Material ejected from the heated spot creates a molecular plume of surface materials in front of the spot. Energy from the laser is insufficient to dissociate molecules or spawn significant ionization, so the plume retains the molecular composition of the target. The melted spot becomes a high-temperature blackbody source. As the blackbody radiation passes through the ejected plume, molecular and atomic absorption occur in the plume materials. Bulk molecular and atomic composition of the surface material is investigated by using a spectrometer to view the heated spot through the ejected material. A system concept is shown in Figure 2-1.

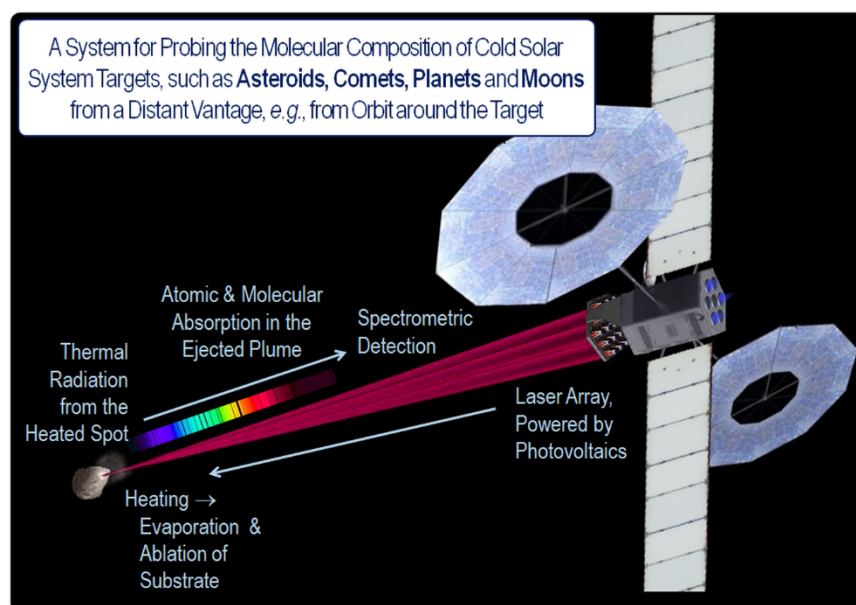


Figure 2-1: The diagram is titled, “A System for Probing the Molecular Composition of Cold Solar System Targets, such as Asteroids, Comets, Planets and Moons, from a Distant Vantage, e.g. from Orbit around the Target”. The diagram shows a spacecraft orbiting an asteroid. The spacecraft includes a main body, which is a hexagonal prism. Mounted on one end of the prism is a gimbel that supports a flat, hexagonal array of 19 laser emitters. Protruding from two opposite faces of the main spacecraft body are two flat, segmented thermal radiators, used to dissipate heat from the spacecraft. Protruding from two other opposite faces of the main spacecraft body are two flat, circular solar arrays which provide power to spacecraft components. The diagram illustrates laser beams emanating from each element in the laser array. The laser beams emanating from the laser array converge on an asteroid that is apparently located at a significant distance from the spacecraft.

The distant asteroid appears as a rocky body, and there is an indication that the focused laser beams are heating a spot on the asteroid's surface. A diffuse plume of evaporated material is depicted near the asteroid, around the area of the heated spot.

2.2 Comparisons to Existing Methods of Remote Composition Analysis

The new method is referred to as Remote Laser Evaporation Molecular Absorption (R-LEMA) spectroscopy. A laser positioned at a remote distance from the target is used to heat the target to the point of evaporation, but not dissociation or ionization. Evaporated material retains the molecular composition of rocky materials in the target, and infrared absorption in the plume of evaporated materials serves as the basis for molecular spectroscopy. R-LEMA spectroscopy offers a complementary approach to current 'stand-off' approaches for composition analysis. Comparisons to existing approaches can help elucidate the uniqueness of R-LEMA.

2.2.1 Laser-Induced Breakdown Spectroscopy (LIBS)

One currently used stand-off approach is Laser-Induced Breakdown Spectroscopy (LIBS) (Miziolek *et al.*, 2006). This technology has been thrust into the public consciousness due to its deployment on the Mars Curiosity rover, dubbed the 'ChemCam' (Demtröder, 2013, Sallé *et al.*, 2004). LIBS uses a pulsed laser with optics that can focus on targets within ~10 m of the rover. The laser pulses deliver a flux exceeding 10 TW/m^2 on the target, which is sufficient to dissociate molecules and create an atomic plasma from materials in the solid target. Light emitted from the plasma is delivered to a series of three spectrometers covering the range 240-850 nm. Atomic composition is derived from the recorded spectra (Sallé *et al.*, 2004). Standoff distance for LIBS on the Curiosity rover is limited by the strength of characteristic emission, and distances greater than ~10 m are problematic. Additionally, the LIBS detector performs atomic composition analysis by observing characteristic emission spectra from the plasma in visible and near-infrared (Vis/NIR) wavelengths. Molecular composition is not available, since the energy delivered to the target by the laser is sufficient to ionize rocky materials. Additionally, LIBS sensors do not cover mid- and long-wave infrared wavelengths, which is where most absorption due to molecular rotation and vibration occur.

2.2.2 Laser-Induced Thermal Emission (LITE) Spectroscopy

Laser-Induced Thermal Emission (LITE) spectroscopy is also capable of probing molecular composition remotely (Sallé *et al.*, 2005; Lin *et al.*, 1988). LITE uses a relatively low-power laser to heat materials in the target to a temperature that is perceptibly higher than the environment. An infrared imaging system focuses radiation from the target onto an infrared spectrometer. Materials in the target emit blackbody radiation with diagnostic spectral features in infrared wavelengths that arise from rotational and vibrational movements of molecules. LITE spectroscopy is theoretically capable of operating at very large stand-off distances, limited mostly by laser power. LITE spectroscopy is typically limited to molecular composition analysis, due to low emitted signal in optical wavelengths, where characteristic emission occurs.

A strategy similar to LITE was utilized by the Deep Impact mission. A large amount of material was ejected from the comet by the impact. The cloud of ejected debris was pushed by solar radiation pressure into the comet's coma. The ejected material was heated by solar radiation (rather than a laser) to ~235 K, and the heated material then emitted blackbody energy peaking

near 12 μm . ‘Solar-illuminated emission spectra’ in the range 5.2-38.0 μm were recorded from the Spitzer Space Telescope in low-Earth orbit, at a distance of ~ 0.75 AU from the comet (Lisse *et al.*, 2006; A'Hearn *et al.*, 2005). Molecular composition of materials in the coma was inferred from the mid- and long-wave infrared (MWIR and LWIR) spectra.

2.2.3 Remote Laser Evaporative Molecular Absorption (R-LEMA) Spectroscopy

The unique aspect of R-LEMA is the idea of ‘backlighting *absorption*’, in contrast to existing methods that rely on detecting energy that is *emitted* by the target material. By measuring absorption spectra using an infrared spectrometer, the R-LEMA system provides a unique and complementary approach to remote molecular composition analysis. For example, in comparison to LIBS (10 TW/m², molecular dissociation, ionization), R-LEMA uses ~ 10 MW/m², which is insufficient to dissociate most geologic molecules, allowing molecular composition analysis. R-LEMA operates in thermal infrared wavelengths. R-LEMA standoff distances (many kilometers) are also envisioned to be much greater than LIBS. R-LEMA and LITE also have differentiating features. LITE relies on energy emitted by the target, whereas R-LEMA creates an artificial source for backlighting spectroscopy. Each system will require a determination of background spectrum for comparison to the spectrum due to the target.

3. NASA MISSION APPLICATIONS

3.1 Utility for Asteroid Redirect Mission (ARM)

The ability to probe molecular composition of cold objects from a distance has specific advantages over existing technologies. One obvious benefit of R-LEMA would be stand-off molecular composition analysis of solar system bodies, *e.g.*, in a scenario such as NASA’s proposed Asteroid Redirect Mission (ARM) (Brophy and Muirhead, 2013). ARM mission objectives include identifying, capturing and redirecting an entire small, near-Earth asteroid to the Earth-Moon system by the first half of the next decade. The re-directed asteroid would be placed in a stable orbit that allows for human exploration and commercial utilization of the asteroid. There is a natural synergy between ARM and the proposed R-LEMA system. An ARM mission could incorporate R-LEMA to perform high spatial resolution surface bulk molecular composition analysis and mapping of the asteroid. No landing or Touch-and-Go (TAG) maneuvers are required for R-LEMA, vastly simplifying mission requirements. Proposed system architecture for R-LEMA aboard ARM includes using a directed-energy beam to heat a spot on the asteroid to the vaporization point of crustal rocks, and to capture high-fidelity spectral measurements for molecular compositional analysis. Focusing on a single area for an extended time would create a borehole or trench, allowing shallow sub-surface molecular composition profiling beneath the regolith. Subsurface composition profiling is not performed with any existing remote sensing method that is used for interrogating the composition of asteroids and comets.

With an R-LEMA system aboard an ARM spacecraft, additional science objectives could also be pursued. The ejected plume creates a reactionary thrust that could be exploited for orbit alteration in impact avoidance scenarios or asteroid capture missions. Numerous studies have confirmed the efficacy of low-thrust approaches using laser ablation for orbit alteration (Zhang, *et al.*, 2016; Lubin *et al.*, 2014; Lubin *et al.*, 2015; Colombo *et al.*, 2009; Gibbings *et al.*, 2011). An Earth-orbiting directed energy system could be used for debris mitigation, for example by mounting a directed energy system on the International Space Station. Directed energy beams could also be used for beamed power delivery, including beamed propulsion for deep space

missions (Lubin *et al.*, 2015). The proposed system could be used in a ‘search-LIDAR’ scanning mode to illuminate dark targets, and could aid discovery of smaller near-Earth asteroids that are increasingly difficult to detect with passive sensors (Riley *et al.*, 2014).

3.2 Mission Design Architecture

A ‘baseline’ system is presented, based on the availability of 100 kW (electrical) as a feasible and fundable option. Details of the design are described in this report, as they relate to the main elements of the spacecraft, namely, spacecraft propulsion, photovoltaic panels, laser array, and radiator as well as the parameters of the launch vehicles under consideration. The objective is to design a system that will enable a spacecraft with a 1 m to 4.5 m diameter laser phased array to arrive at an NEA and characterize its composition, with potential for an extended mission to deflect the NEA from a potentially hazardous trajectory. The laser phased array is described, along with a lower risk potential fallback—a close packed focal plane array of fiber lasers. The propulsion for the LEO to NEA portion of the mission is made possible with a high-power solar electric propulsion (SEP) system (Brophy and Muirhead, 2011). The solar photovoltaic (PV) arrays convert power from the sun to provide system power. PV panels will originally be stowed for launch and will deploy upon reaching low-Earth orbit to provide a required 100 kW electrical power from two 15 m diameter ATK MegaFlex panels. Even larger power is possible within the launch mass and shroud sizes available. The system will utilize ion engines to propel the spacecraft from LEO to an NEA, as proposed in JPL’s ARM program. The system aims to stay within the same mass and launch constraints as ARM and use much of the same propulsion technology. The laser efficiency determines the laser power obtained from the PV arrays; 35 kW of laser power would be produced at 35% efficiency and 50 kW at 50%. The 35 kW estimate is based on the current efficiency (35%) of existing technology of the baseline Ytterbium laser amplifiers and thus provides for the worst case, while the 50 kW estimate is based on near-term technological improvement within the next 5 years. A passive cooling radiator with z-folded arrays will be used to reject waste heat and maintain the spacecraft temperature at an operational 300 K.

3.2.1 Spacecraft Design Principle

The basic design principle is to utilize a cylindrical bus with the lateral center of gravity close to the centerline (Kosmo *et al.*, 2014). PV panels will be stowed at the back of the bus until deployment, and the hexagonal laser array will be mounted on a gimbal at the front of the spacecraft (Fig. 2). Radiator panels will deploy up and down (perpendicular to the bus) and will rotate about their axis so as to remain perpendicular to the sun in order to maximize radiator efficiency. Ion engines are located at the back of the spacecraft. Critical components are outlined in subsequent sections of this report.

3.2.2 Photovoltaic (PV) Panels

Two 15 m diameter MegaFlex PV arrays, manufactured by ATK Aerospace Systems in Goleta, CA, will be used to obtain the baselined 100 kW power solution, shown in Figure 3-1. Extensive testing has been conducted on MegaFlex technology and the MegaFlex arrays have a high Technology Readiness Level (TRL) (Murphy *et al.*, 2014). The spacecraft will utilize ion propulsion to spiral out from LEO to its target (Kosmo *et al.*, 2015). Ion engines are proposed for the mission because they are between five and ten times more efficient than engines using conventional chemical propellants, depending on the type of ion engine.

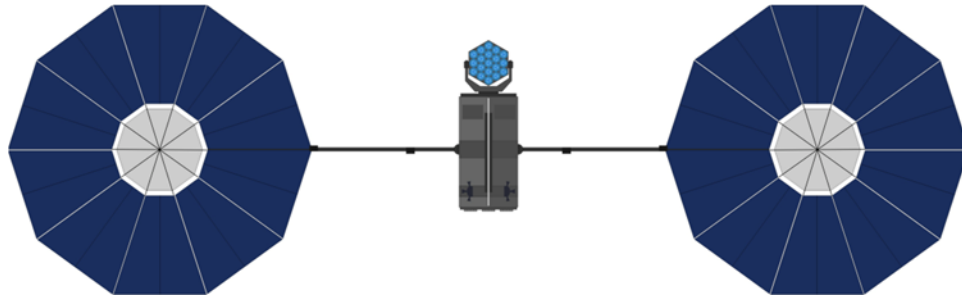


Figure 3-1: Conceptual design of the deployed spacecraft with two 15 m PV arrays that produce 50 kW each at the beginning of life for a total of 100 kW electrical, ion engines at the back, and the laser array pointed directly at the viewer. A 2 m diameter laser phased array is shown with 19 elements, each of which is 1-3 kW optical output. A 2 m diameter optical system is one of the possibilities for a hypothetical mission. More elements are easily added to allow for scaling to larger power levels. A 1.0-4.5 m diameter array is feasible; no deflection will come from a larger optic, just additional range from the target.

3.2.3 Laser Array Design

The proposed baseline optical system consists of 19 individual optical elements in a phased array. A single element concept is shown in Figure 3-2. A significant benefit of utilizing an array of phase-locked laser amplifiers is that it is completely modular and thus scalable to much larger systems, and allows for a greater range than would a close packed array with a single optic. Focusing and beam steering are achieved by controlling the relative phase of individual laser elements. Rough pointing of the array to the target is determined by spacecraft attitude control and gimbal pointing of the optics. Laser tips behind each optical element are mounted on 6-axis micro-positioner hexapod; lateral movement of the laser tips behind each lens provides intermediate pointing adjustment for individual array elements. Each fiber tip is supported on the hexapod and can be augmented with a z-axis rapid position controller if needed. It is not clear if this is needed currently. Precision beam steering is accomplished by coordinated phase modulation across the array by z-position control of the fiber tips as well as by electronic phase modulation. Each fiber is fed with a phase-controllable laser amplifier. Phase feedback from in front of the lens array to each phase controller provides a signal for beam formation adjustment (spot focus). Phase alignment is maintained to within $\lambda/10$ 1-sigma RMS across the entire array, assuming adequate phase controller system response (Hughes *et al.*, 2014).

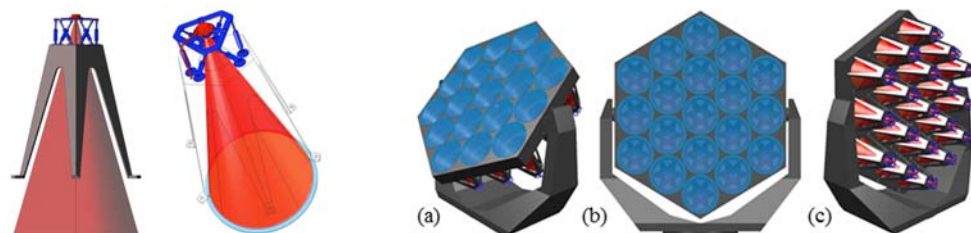


Figure 3-2: Single element of laser phased array, showing fiber-tip actuator for mid-level pointing control and rough phase alignment. The single elements are mounted into a hexagonal array frame with a baseline of 19 elements. The array is depicted at: (a) at 45 degrees, (b) face on, and (c) from the back.

The spacecraft will be capable of outfitting a laser array with an aperture between 1 m and 4.5 m. Changing the aperture would not change the power of the laser; thus the solar arrays and radiator could be of the same dimensions, regardless. The difference in mass between the 1 m array and the 4.5 m array is not significant enough to pose new constraints. The benefit of a larger aperture is that the range of the laser from the target for a given power scales with the linear size of the optical aperture. For example, the range of a 3 m array is three times greater than that of a 1 m array. The benefit of having a longer range is that it allows the spacecraft to remain clear of the debris of the ejected material. The debris flux ($\text{kg/m}^2 \text{ s}$) that hits the spacecraft drops as the square of the distance to the target. However, the total amount of particle debris (kg/s) on the optic is independent of distance since the range is proportional to the optic diameter, and the area of the optic is proportional to the square of the diameter. The main drawback of the larger aperture is a higher associated cost. The decision, thus, is dependent on funding and other mission specifics. Even sub-meter diameter optics are feasible if needed for specific missions.

The laser array will be placed on a gimbal to eliminate any potential issues with fuel usage in maneuvering the spacecraft, as depicted in Figure 3-2. Further, it will allow for much greater flexibility in mission execution. This is imperative because the laser will have to raster scan the asteroid in order to maximize thrust, prevent burn through, and de-spin the asteroid if needed. Though much of this can be done with electronic steering, using a gimbal will be more energetically efficient than pointing the spacecraft. A gimbal would also be beneficial in the event that the spacecraft needs to orbit the target. Further, the added flexibility due to the gimbal mitigates risk by allowing the system to target smaller pieces of the asteroid that may get dislodged and pose a threat to the spacecraft. The gimbal will allow for two degrees of freedom because the angular orientation around the boresight of the spot on the asteroid is not a significant concern. This will be cheaper, easier to manufacture, and lighter than a system with greater degrees of freedom.

3.2.4 Secondary Optical Configuration of the Laser Array

If necessary, a fallback option is to implement a hexagonal close packed focal plane array of laser fibers with a conventional optic such as a reflecting telescope instead of a phased array. A conceptual diagram is shown in Figure 3-3. This system would consist of 19 circular fibers, each 25 μm in diameter with a sheath (cladding) around the inner core. The cladding will be 37.5 μm thick so that the center-to-center spacing of adjacent laser fibers is 100 μm . The thickness of the cladding may be increased if power leakage and cross talk is an issue. As with the phased array design, each fiber is attached to an amplifier; however, the fibers are close packed in the focal plane and utilize one larger hexapod and the lasers are NOT phase locked for simplicity. The close packed array will produce 19 individual spots on the target, separated center to center by the ratio of the target distance to optical size times the fiber spacing in the focal plane. For the baseline of 1.5 kW per amplifier, each fiber will illuminate the target with a spot diameter of approximately 12 mm and a center to center spacing of approximately 50 mm; however, this can be changed depending on the optical design. This option carries a lower risk, higher initial TRL, lower cost, and can also be implemented more rapidly. In addition, it requires the spacecraft to be significantly closer to the target than would be required with a phased array. The plan is to pursue both the phased array and the close packed array, and down select depending on specific mission parameters.

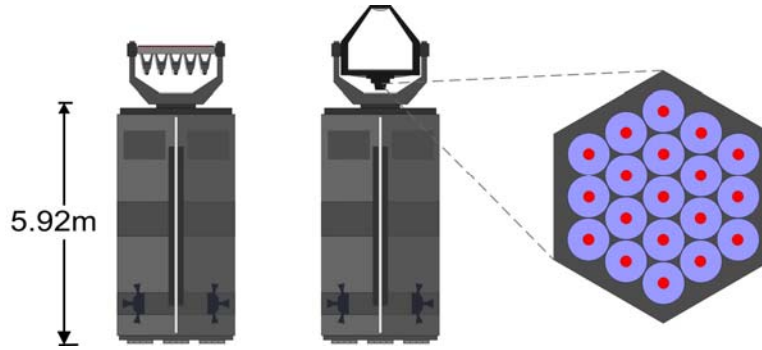


Figure 3-3: Comparison view of mounted laser phased array and a close-packed array. The hexagonal close-packed focal plane array of 19 laser fibers is mounted in the focal plane frame. Laser fibers have a diameter of 25 μm , the cladding around each of which is 37.5 μm thick.

3.2.5 Spacecraft Thermal Management

Thermal radiators are essential to spacecraft design so as to minimize incident radiation and maintain the spacecraft and its components at a functional temperature. The efficiency of the radiator can be determined by Equation 3.2.5-1, which relates the thermal flux to the rejected heat and area of the radiator:

$$F = \dot{Q}/A = \epsilon \sigma T^4 \quad 3.2.5-1$$

where ϵ is the emittance of the surface, σ is the Stephan-Boltzmann constant, T is the temperature, \dot{Q} is the heat rejected, A is the area, and F is the flux (Aaron, 2002). The baseline radiator will be coated in AZ-93 white paint, which has a high emittance of 0.91 ± 0.02 (or conservatively, 0.89) and a low alpha, as it only absorbs 14-16% of incident sunlight on the spacecraft. The goal is to maintain a temperature of 300 K, as both the laser and onboard control electronics are operational at this temperature. At this temperature, the radiator can reject an idealized outward flux of 408 W/m². When taking into account the incident radiation, using a solar constant of 1362 W/m² and a maximum 16% absorptance, the net flux of energy across the surface of the radiator is approximately 190 W/m². The baseline is to prevent direct solar illumination of the radiator.

The area of the radiator must be determined by thermal analysis, and is dependent on the desired operating temperature, heating from the environment, interactions with other surfaces of the spacecraft (*e.g.*, solar arrays), and the highest estimate (worst case) satellite waste heat. The waste heat in this case is dependent on the efficiency of the laser amplifiers—35% or 50% as mentioned. The worst-case estimate (35% efficiency) requires 65 kW to be rejected as waste heat for a 100 kW electrical input assuming virtually all the power goes to the laser (which is approximately correct during laser firing). The required area A can be determined by Equation 3.2.5-2, which relates the rejected heat to the area of the radiator and the net outward flux:

$$\dot{Q}_{\text{rejected}} = A F_{\text{net}} \quad 3.2.5-2$$

where F_{net} is the net outward flux and \dot{Q} is the heat rejected. Given these parameters, the maximum required area of the radiator is $\sim 341 \text{ m}^2$ for a 35% efficient laser amplifier. For a 50% efficient laser, a radiator area of $\sim 262 \text{ m}^2$ is required. The model assumes that either a pumped liquid cooling loop or an advanced heatpipe would be used to transfer the heat from the laser to the radiator as is currently done now in the other uses of these laser amplifiers.

A passive cooling z-folded radiator consisting of two deployable panels will be used in order to provide a sufficient surface area over which to emit the waste heat generated by the system. Each panel z-folds out into six segments, each of which further folds out into two additional segments, making 18 segments in total for each panel. The panels will rotate about their axes to maximize efficiency by remaining perpendicular to the sun and by radiating out of both sides. Each segment will be 2.2 m by 2.2 m, yielding a total area of 348 m². Note that the radiators radiate out of both sides and that there are two radiator panels. These values are approximate; a more detailed radiator design would be required as part of an overall mission design. The expectation is that, by the time of any mission start, significant increases in laser efficiency will have been achieved, thus reducing the required radiator size. Sun shades may also be used to limit solar absorption and thus allow for greater efficiency. The current mass to power ratio for radiators is about 25 kg/kW for the ARM system.

3.2.6 Potential Launch Vehicles

The objective is to assess which launch vehicle is the most feasible and will provide the greatest performance given the mission directives. The launch systems in consideration are Atlas V 551, Space Launch System (SLS) Block 1, Falcon Heavy, or Delta IV Heavy. These are likewise the launch systems in consideration for JPL's Asteroid Redirect Mission, which calls for a payload of comparable parameters (Brophy and Muirhead, 2013).

Table 3-1. Parameters of various launch vehicles in consideration. The table considers four potential launch vehicles (columns), and four parameters of interest (rows), and provides information for each of the parameters specific to the launch vehicle.

Parameter	Atlas V 551	SLS Block 1	Falcon Heavy	Delta IV
Payload Mass to LEO	18 500 kg	70 000 kg	53 000 kg	28 790 kg
Cost per unit mass to send into LEO	\$13 200 / kg	\$18 700 / kg	\$1 890 / kg	\$13 000 / kg
Diameter of Payload Fairing	5.4 m	8.4 m	5.2 m	5 m
Status	Flight proven	Development— First Expected Flight: 2017	Development— First Expected flight: 2015	Flight proven

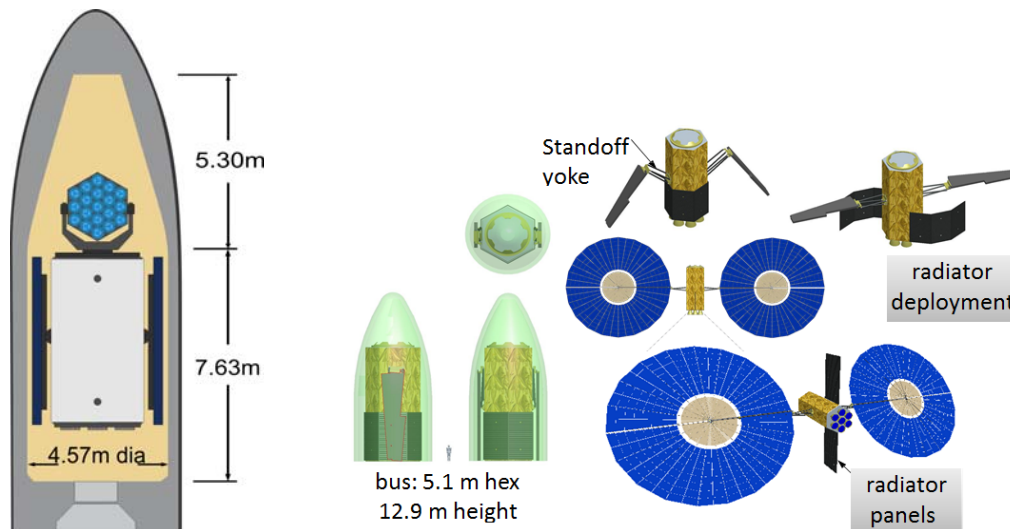


Figure 3-4: Stowed view of the spacecraft, in a 5 m fairing. Deployment scenario for 30 m diameter 450 kW (pair) of ATK Megaflex panels from packing in an SLS fairing. Radiators are also shown as one possible option. Once outside the fairing, solar arrays are unfolded. Solar arrays are depicted larger than the emitter array, allowing for less efficient PV conversion.

The spacecraft will fit within the payload fairing of any of the proposed launch systems, as depicted in Figure 3-4. As is evident from the data in Table 3-1, the SLS Block 1 has the highest capabilities, though also requires the highest cost. The Falcon Heavy demands the smallest cost per unit mass, and has capabilities between that of the Atlas V and SLS Block 1. While the Atlas V 551 and Delta IV Heavy have previously undergone successful missions, the SLS Block 1 and Falcon Heavy are projected to be flight-proven within the timescale of the mission. As with the Asteroid Redirect Mission, it is possible to compensate for the lower capabilities of the Atlas V by using the SEP system to spiral out of Earth's orbit and escape from Earth using Lunar Gravity Assist (LGA); however, this process of spiraling out and using LGA will take an additional 1 to 1.5 years of flight. All of these factors must be taken into consideration to choose the most effective launch system for the mission.

3.3 Extended Mission Capability of R-LEMA System

Asteroid impacts pose a clear threat and future advancement to minimize this threat requires effective mitigation strategies. A wide array of concepts for asteroid deflection has been proposed. Several detailed surveys of threat mitigation strategies are available in the literature, including Sanchez-Quartielles *et al.* (2007), Belton *et al.* (2004), Gritzner and Kahle (2004), and Morrison *et al.* (2002). Currently proposed diversion strategies can be broadly generalized into six categories.

(1a) Kinetic impactors, without explosive charges. An expendable spacecraft would be sent to intercept the threatening object. Direct impact could break the asteroid apart (Melosh and Ryan, 1997), and/or modify the object's orbit through momentum transfer. The energy of the impact could be enhanced via retrograde approach, *e.g.* McInnes (2004).

(1b) Kinetic impactors, with explosive charges. Momentum transfer using an expendable spacecraft could also be enhanced using an explosive charge, such as a nuclear weapon, *e.g.* Koenig and Chyba (2007).

(2) Gradual orbit deflection by surface albedo alteration. The albedo of an object could be changed using paint, *e.g.* Hyland *et al.* (2010). As the albedo is altered, a change in the object's Yarkovsky thermal drag would gradually shift the object's orbit. Similar approaches seek to create an artificial Yarkovsky effect, *e.g.* Vasile and Maddock (2010).

(3) Ion beam deflection (IBD) or ion beam shepherd (IBS) where high speed ions, such as the type used for ion thrusters, are directed at the asteroid from a nearby spacecraft, to push on asteroid and thus deflect it. (Bombardelli *et al.*, 2016; Brophy, 2015; Bombardelli, *et al.*, 2013; Bombardelli and Peláez, 2011).

(4) Direct motive force, such as by mounting a thruster directly to the object. Thrusters could include chemical propellants, solar or nuclear powered electric drives, or ion engines (Walker *et al.*, 2005).

(5) Indirect orbit alteration, such as gravity tractors. A spacecraft with sufficient mass would be positioned near the object, and maintain a fixed station with respect to the object using onboard propulsion. Gravitational attraction would tug the object toward the spacecraft, and gradually modify the object's orbit (Mazanek, *et al.*, 2015; Wie, 2008; Wie, 2007; McInnes, 2007; Schweickart *et al.*, 2006; Lu and Love, 2005).

(6) Expulsion of surface material such as by robotic mining. A robot on the surface of an asteroid would repeatedly eject material from the asteroid. The reaction force when material is ejected affects the object's trajectory (Olds *et al.*, 2007).

(7) Vaporization of surface material. Like robotic mining, vaporization on the surface of an object continually ejects the vaporized material, creating a reactionary force that pushes the object into a new path. Vaporization can be accomplished by solar concentrators (Vasile and Maddock, 2010), lasers deployed from the ground (Phipps, 2010), or lasers deployed on spacecraft stationed near the asteroid (Maddock *et al.*, 2007; Park and Mazenek, 2005; Gibbings *et al.*, 2013; Phipps and Michaelis, 1995; Campbell, 2000; Vasile *et al.*, 2013). One study (Kahle *et al.*, 2006) envisioned a single large reflector mounted on a spacecraft traveling alongside an asteroid. The idea was expanded to a formation of spacecraft orbiting in the vicinity of the asteroid, each equipped with a smaller concentrator assembly capable of focusing solar power onto an asteroid at distances near ~1 km (Vasile and Maddock, 2010). An R-LEMA system could be utilized for asteroid orbit alteration, without any modification whatsoever from its primary intended purpose of compositional analysis. A discussion of the relative deflection capability of R-LEMA and other methods is provided in Section 5.7.1.

4. CONCEPT EVALUATION APPROACH

4.1 End-to-End System Model

The system readiness of R-LEMA at the beginning of the NIAC Phase I research was TRL-1. In order to extend the system readiness, the NIAC Phase I research developed theoretical analysis of the underlying physical principles that support the system concept. The analysis consists of theoretical models of sub-system operation, including laser optical propagation model, a target thermal model, estimation of evaporation of target material and resulting plume density, molecular absorption of radiation from the heated spot in the ejected plume, and estimation of the absorption lines that would be viewed by a spectrometer based on molecular cross sections of expected asteroid materials and absorption of thermal radiation in the ejected plume. Each sub-system model feeds into successive stages to provide an end-to-end model of the overall sensor system.

4.2 Evaluation of the Sensor System Concept

Based on the end-to-end model, simulations have been developed for various operational scenarios. Using a selected laser power, with a specific optical configuration, and assuming a target distance and specific composition, numerous cases are explored. Evaluation of the sensor system is based on the expected absorption profile for hypothetical operational settings. The key indicator of sensor system capability in any setting is the amount of absorption that is expected at diagnostic wavelengths for the various materials expected to comprise asteroids. Results from extensive simulations of molecular absorption profiles with laser heating indicate high probability for success of molecular composition analysis with currently available technology. Deep absorption lines are indicated for all materials studied, and in every reasonable operational setting that was simulated. Details of the end-to-end model and simulation results are described in Section 5.

5. TECHNICAL DETAILS SUPPORTING CONCEPT FEASIBILITY

5.1 Laser Optical Propagation Model

5.1.1 Laser Phased Array Concept

A baseline design (Kosmo *et al.*, 2014) for beam formation and steering is shown in Figure 5-1. A seed laser supplies a reference source for the array of fiber amplifiers. Rough pointing of the array to the target is determined by spacecraft attitude control. Fiber tips behind each optical element are mounted to micro-positioner actuators; lateral movement of the laser tips behind each lens provides intermediate pointing adjustment for individual array elements and beam steering. Precision beam steering and beam formation (spot focus) is accomplished by coordinated phase modulation across the array. Feedback from wavefront sensors in front of the optical elements is used to adjust the input phase to each amplifier. This scheme requires a phase reference signal to be present at the exit aperture of each optical element. Ideally, the reference signal would consist of parallel wavefronts travelling along the target axis. Geometric constraints require novel approaches to generation and use of the phase reference signal (Vorontsov *et al.*, 2009)

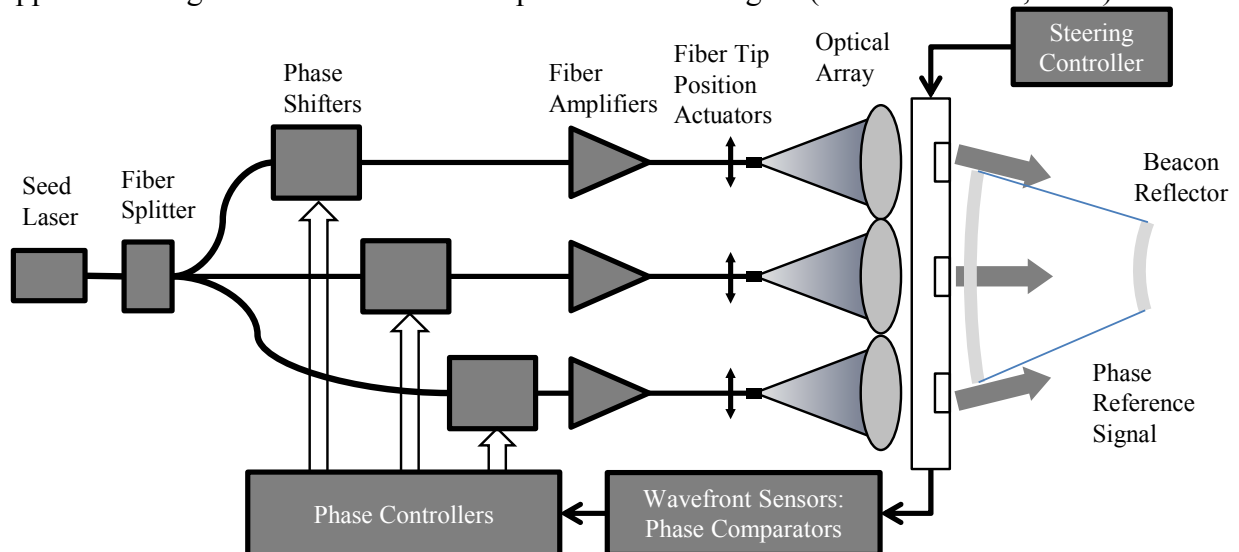


Figure 5-1: Conceptual block diagram of laser phased array architecture based on kW-class laser fiber amplifiers. The seed laser provides a base signal to each fiber

amplifier, through individual phase controllers. Wavefront sensors in front of the emitters provide feedback to the phase controllers, which results in beam steering, focus and overall control.

5.1.2 Far-Field Intensity Model of Phased Array Beams

The interference pattern and resulting far-field intensity distribution of multiple emitters in a phased-array design can be determined by scalar diffraction theory. Table 5-1 defines terms commonly used in the antenna literature (Balanis, 2016; Hansen, 2009). For simplicity, simulations in this paper are based on a planar, rectangular array of square emitters with constant, close-packed spacing. Simulations are possible with other geometries by modifying the array pattern contribution.

Table 5-1. Terms that are commonly used in the antenna literature, including units associated with each term used for simulations presented in this paper. The table contains symbols, the symbol interpretation, and units for each symbol (columns), and provides details for all symbols used (rows).

Symbol	Interpretation	Units
λ	Nominal emitter wavelength	μm
d	Nominal element spacing (array pitch)	μm
θ	Angular variable (viewing angle away from normal to emitter array plane)	rad
E	Complex far-field amplitude	V/m
I	Far-field beam intensity	W/m^2
k	$2\pi/\lambda$	μm^{-1}
a	Aperture opening size	μm
N	Number of emitters in a single dimension of an array	dimensionless

The complex far-field amplitude for a flat, linear array of emitters in phase alignment is given by Equation 5.1.2-1, which relates the far-field intensity to a sum of complex frequencies from each emitter when no phase mis-alignments are present:

$$E(\theta) = E_0 \cdot \frac{e^{[i \cdot k \cdot a \cdot \sin(\theta)]} - 1}{i \cdot k \cdot \sin(\theta)} \cdot \sum_{p=0}^{N-1} e^{[i \cdot k \cdot p \cdot d \cdot \sin(\theta)]} \quad 5.1.2-1$$

Given the complex amplitude, the far-field beam amplitude for the linear array is then given by Equation 5.1.2-2, which related the far field beam intensity to the beam amplitude:

$$I(\theta) = |E(\theta)|^2 \quad 5.1.2-2$$

For a 1-D linear array, the far-field beam intensity for a square array with beam intensity $I_x(\theta)$ along one axis and $I_y(\psi)$ along a perpendicular axis is given by 5.1.2-3, which relates the intensity of the combined beam from viewing angles θ and ψ to the individual linear intensities:

$$I(\theta, \psi) = I_x(\theta) \cdot I_y(\psi) \quad 5.1.2-3$$

Equations 5.1.2-1 through 5.1.2-3 can be used to determine the far-field intensity pattern of a planar array of emitters. The equation assumes perfect mechanical alignment, as well as perfect frequency, amplitude and phase control for every emitter in the array. A simulation was

performed, based on Equations 5.1.2-1 through 5.1.2-3 for a 5 by 5 array. Figure 5-2 shows 1-D and 2-D far-field beam patterns.

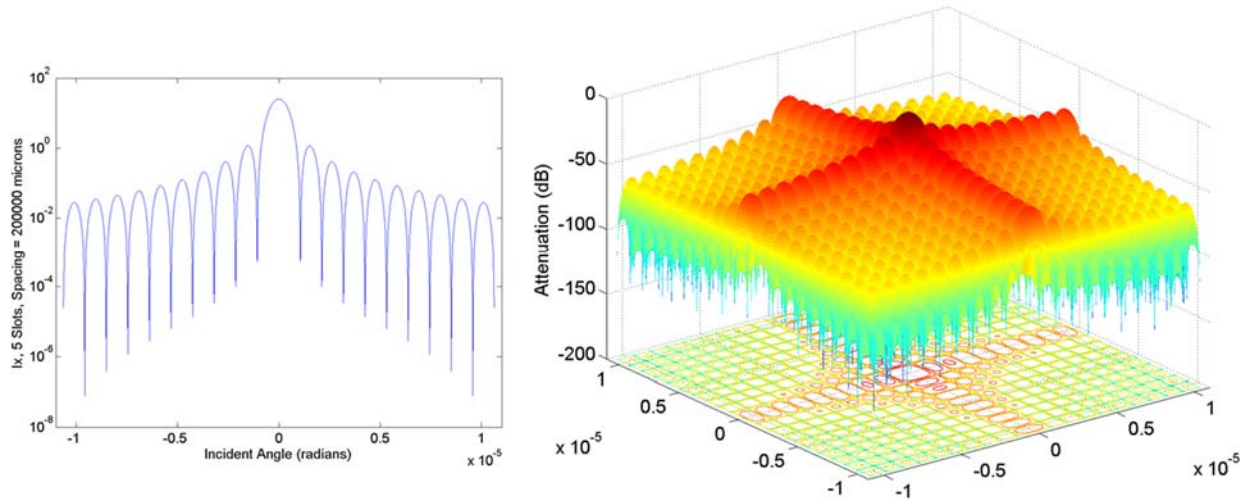


Figure 5-2: Baseline simulation results for a 5 by 5 close-packed array of square emitters in phase alignment. Each emitter is a 20 cm by 20 cm square ($a = d = 20$ cm), so total aperture is 1 m, $N = 25$, and the nominal emitter frequency is set to $\lambda = 1.06 \mu\text{m}$. The far-field beam pattern for such an array with no phase perturbations is shown in a contour plot, and cross section. The vertical axis of both plots indicates intensity, showing additive amplification in the center of the combined beam pattern. These results would only be attained by having perfect mechanical alignment and perfect frequency, amplitude and phase control of the every emitter in the array.

5.1.3 Effects of Phase Perturbations in the Optical Model

Design requirements for a laser phased array can be investigated by introducing perturbations to the baseline optical model given in Equation 5.1.2-1. In practice, the array will have imperfections in mechanical alignment that will introduce single-emitter pointing errors and phase misalignments. Alignment flaws manifest as static perturbations to the far-field intensity. An operational system will also have vibrational modes, thermal variations and other sources of phase error that contribute temporal perturbations to beam formation and pointing. Figure 5-3 depicts the effects of each component on phase alignment. Assembly defects are static, uncorrelated phase and amplitude perturbations. Vibrational modes introduce time-varying phase and amplitude perturbations that are correlated across the array. Thermal and other variations contribute to uncorrelated, time-varying phase and amplitude perturbations.

Equation 5.1.2-1 can be modified to include additive fixed and time-varying phase misalignments, representing the two mechanical scenarios in Figure 5-3. The complex far-field amplitude for a linear array of emitters with static (E_f) and time-varying (E_t) phase misalignments at each emitter is given in Equation **Error! Reference source not found.**, which relates the far-field intensity to a sum of complex frequencies from each emitter when fixed and dynamic phase mis-alignments are present:

$$E(\theta, t) = \frac{e^{[i \cdot k \cdot a \cdot \sin(\theta)]} - 1}{i \cdot k \cdot \sin(\theta)} \cdot \sum_{p=0}^{N-1} e^{\{i \cdot [k \cdot p \cdot d \cdot \sin(\theta) + E_f(p) + E_t(p, t)]\}} \quad 5.1.3-1$$

Phase errors due to assembly imperfections are included in Equation 5.1.3-1 as fixed differences at each emitter, $E_f(p)$. Assembly errors can be modeled by random assignment of a fixed phase difference to each element in the array. For the simulations presented in this paper, fixed phase differences are drawn randomly from a normal distribution with zero mean and a specified standard deviation, written as in Equation 5.1.3-2, which relates a normally-distributed random variate to the inverse normal cumulative distribution function of a uniformly-distributed random variate:

$$E_f(p) = \text{invNorm}(\text{rand}(), \text{mean} = 0, \text{standard deviation} = \sigma) \quad 5.1.3-2$$

Standard deviation represents the variation among fixed alignment differences, and is typically stated in terms of a fraction of a single cycle at the nominal emitter frequency. Fixed differences of precisely one cycle are phase aligned, so the alignment requirement can be stated as modulo- 1λ .

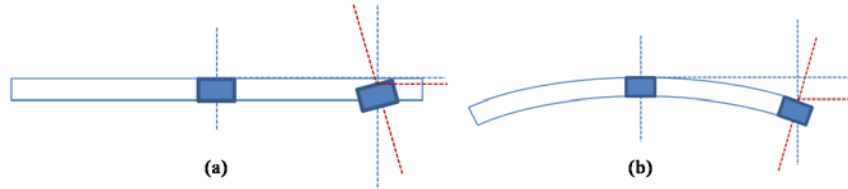


Figure 5-3: Illustration of the effects on phase alignment of (a) mechanical misalignment of optical elements, and (b) first-mode structural vibration. If a single element is mis-aligned, a fixed phase error due to displacement of the emitter from the nominal focal plane. Structural vibrations will also create dynamic phase errors between emitters as the physical position of emitters moves above and below the nominal focal plane.

Fixed alignment differences can be chosen randomly, since they can be viewed as uncorrelated random errors. However, time-varying terms can be both correlated and uncorrelated. Vibrational modes in the structure will create phase misalignments that are correlated among the array emitters. Additional perturbations are also possible, for example due to thermal changes in optical paths or non-linear reactions of optical elements to structural vibrations. Some of these scenarios may result in uncorrelated phase misalignments, which can also be included in the model by adding a series of time-varying terms, *i.e.*, $E_t(p, t)$ in Equation 5.1.3-1 can be a sum representing several components.

5.1.4 Optical Simulation Results

It is well-known that mechanical anomalies on the order of $\sim\lambda/10$ can introduce significant aberrations in optical systems. The simulation results shown in Figure 5-4 represent a laser phased array that includes fixed phase mis-alignments (E_f) at each emitter with a 1σ error of $\lambda/8$. Comparison of these results to Figure 5-3 shows significant beam degradation, with significant power moving from the main peak to side lobes. Also evident is a pointing shift, *i.e.*, the main lobe axis is no longer aligned with the array axis, with a pointing error on the order of $1\ \mu\text{rad}$. A time series of pointing errors is shown in Figure 5-4.

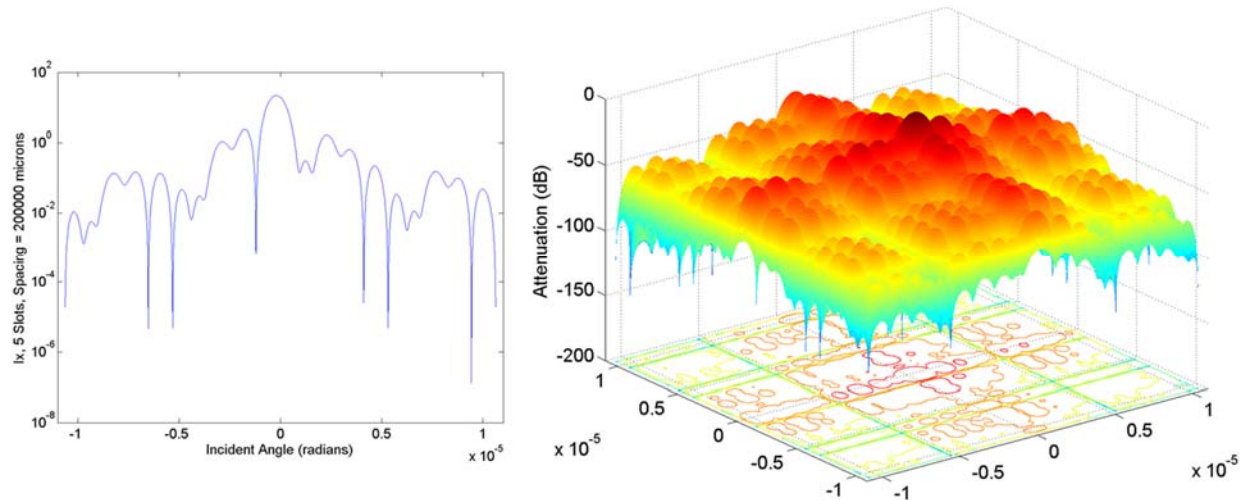


Figure 5-4: Simulation results for a 5 by 5 close-packed array of emitters with static phase perturbations. Again, emitters are modeled as $a = d = 20$ cm, total aperture is 1 m, and the nominal emitter frequency is set to $1.06 \mu\text{m}$ (compare to Figure 5-2). Mis-alignments were randomly assigned to each emitter, with magnitudes drawn from a normal distribution with $1\sigma = 2\pi/8$.

5.1.5 Simulations with Time-Varying Perturbations

In addition to static phase misalignments, the model can incorporate time-varying phase errors, such as induced by structural vibration or thermal variations. Figure 5-5 shows a simulated time series of pointing error, sampled at 1 kHz. As can be seen, the direction of the main lobe is deflected less than $1.8 \mu\text{rad}$. Only uncorrelated phase errors were introduced for the simulation depicted in Figure 5-5. Errors were specified as sinusoids with randomly assigned amplitude, frequency and phase, with magnitudes for each sinusoid parameter drawn from uniform distributions on $[0, 1]$. In the presence of time-varying phase errors, the pointing error is rarely close to 0 rad, but always small compared to the main lobe beam width.

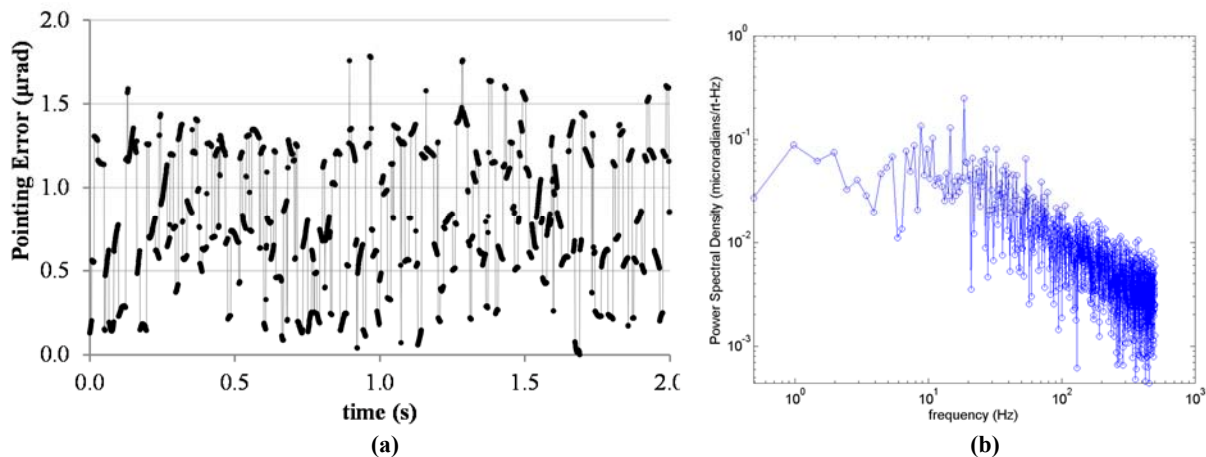


Figure 5-5: Pointing error through time, and as a frequency spectrum, based on a simulated 2 second time series for a 5 by 5 close-packed array of emitters with uncorrelated dynamic phase perturbations across the array. Again, emitters are

modeled as $a = d = 20$ cm, total aperture is 1 m, and the nominal emitter frequency is set to $1.06 \mu\text{m}$. The frequency spectrum was calculated from the 2 second time series.

Simulation results can be compared to simple Ruze theory, with one caveat: the comparison is not strictly appropriate, due to assumptions of correlation sizes in Ruze theory. Comparison to Ruze theory provides some amount of model validation. The simulations agree extremely well with the simple Ruze exponential roll off of forward gain or flux on target. The Ruze equation is given in Equation 5.1.5-1, which relates the ratio of flux on target with phase error over the flux on target without phase error to the phase variance per element:

$$\frac{\langle P \rangle}{P_0} = e^{-\text{Var}(\varphi)} \quad 5.1.5-1$$

where $\text{Var}(\varphi)$ is the variance of the phase per element $\langle P \rangle$ is the expected value of flux on target with phase perturbations, and P_0 is the flux on target with no phase perturbations. Figure 5-6 shows results of two Monte Carlo simulations comparing power roll off to Ruze predictions for two arrays.

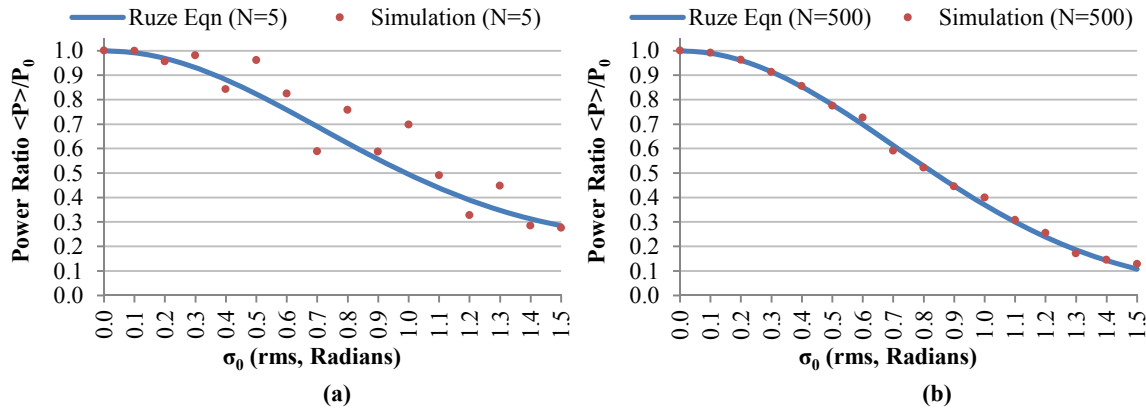


Figure 5-6: Comparison of simulation results to the Ruze equation for average gain fall-off as a function of phase error magnitudes across the array. (a) $N = 5$, with $a = b = 20$ cm and 10,000 simulation runs; (b) $N = 500$ with $a = b = 1$ m and 10,000 simulation runs. Both plots were created with the nominal emitter frequency is set to $1.06 \mu\text{m}$, and show excellent convergence of simulation results to the Ruze relationship.

5.2 Target Thermal Model

To investigate the feasibility of R-LEMA, models of the thermal progression of bolides being bombarded with laser energy have been developed. Simulations include coherently combined laser arrays and tiled-aperture configurations. Model results present a theoretical foundation that supports the proposed method. The core idea of remote composition analysis relies on the ability to heat a distant target to the point of vaporization. The performance of Ytterbium-doped fiber laser amplifiers has improved markedly in recent years, and lightweight systems are now capable of delivering sufficient flux to vaporize very distant targets. Continuous-wave, multi-kW-class devices are now routine and affordable, germinating many novel applications (Zervas and Codemard, 2014). Phased array configurations of laser fiber amplifiers have been

demonstrated in the laboratory (Vorontsov *et al.*, 2009). Alternatively, multiple lasers could be arranged without phase alignment, and individual beams could be focused on adjacent spots on the target. Tiled-aperture configurations are effective, but would be limited to closer targets than phased-array emitters with equivalent base power.

To investigate the feasibility of R-LEMA, models of the thermal progression of bolides being bombarded with laser energy have been developed. A multi-physics model of the thermal progression of a bolide being bombarded with laser energy has been developed, including a detailed derivation of the model (Hughes *et al.*, 2015; Hughes *et al.*, 2016; Lubin *et al.*, 2014; Lubin and Hughes, 2015; Lubin *et al.*, 2016). The thermal model was derived from energy conservation, and includes thermal characteristics of the bolide being bombarded with laser energy.

5.2.1 Energy Conservation Principles During Laser Bombardment of Target

As the laser beam impinges on the target, energy is converted among several forms. The basic equations are derived from energy conservation shown in Equation 5.2.1-1, which relates laser-in power to laser-out power and asteroid internal energy:

$$\text{Power in (laser)} = \text{Power out (radiation + mass ejection)} + \frac{dU}{dt} \quad 5.2.1-1$$

Where U = Asteroid internal energy and dU/dt is effectively from conduction. In the steady state dU/dt is related to laser power as shown in 5.2.1-2:

$$P_{in} = P_{out} + \frac{dU}{dt}, \text{ with } U = \int \rho c_v dv \quad 5.2.1-2$$

Where c_v = specific heat [J/kg-K], and:

F_L = Laser flux [W/m^2] - (*in*), F_{cond} = Thermal conduction [W/m^2] - (*in*), and

F_{rad} = Radiation flux [W/m^2] - (*out*), F_{ejecta} = Ejecta flux [W/m^2] - (*out*).

Assuming $P_{in} = P_{rad} + P_{ejecta} + P_{cond}$, then the surface integral of the sum dotted with the surface normal dA will be zero, as indicated in 5.2.1-3:

$$\iint (F_L - \bar{F}_{rad} - \bar{F}_{ejecta} - \bar{F}_{cond}) \cdot \hat{n} dA = 0 \quad 5.2.1-3$$

Under specific conditions of thermal conductivity, the ejecta flux can be calculated as in Equation 5.2.1-4:

$$\bar{F}_{ejecta} = \Gamma_e H_v \hat{n} = M^{1/2} (2\pi RT)^{-1/2} \alpha_e 10^{[A-B/(T+C)]} H_v \hat{n} \quad 5.2.1-4$$

Where Γ_e is the mass ejection flux [$kg/m^2 s$], and H_v is the heat of vaporization [J/kg]. The heat of fusion, H_f , is included for relevant cases. The heat of fusion is sometimes referred to the heat of sublimation as is sometimes the case for compounds in vacuum. H_f is typically a small fraction of H_v . The mass ejection flux is shown in Equation 5.2.1-5, which uses vapor pressure:

$$\Gamma_e = \frac{M \alpha_e (P_v - P_h)}{\sqrt{2\pi MRT}} = M^{1/2} (2\pi RT)^{-1/2} \alpha_e (P_v - P_h) \quad 5.2.1-5$$

Where:

M = Molar mass [kg/mol]

P_v = Vapor pressure [Pa]

P_h = Ambient vapor pressure = 0 (in vacuum)

α_e = coefficient of evaporation

The models vapor pressure for each element and compound is determined using a semi analytic form known as Antoine coefficients A, B and C in Equation 5.2.1-6:

$$\text{LOG}(P_v) = A - B / (T + C) \quad 5.2.1-6$$

Where A, B and C are unique per element and compound. Hence, the vapor pressure can be restated by Equation 5.2.1-7:

$$P_v = 10^{[A-B/(T+C)]} \text{ and } |F_{\text{Ejecta}}| = M^{1/2} \frac{1}{\sqrt{2\pi RT}} \alpha_e 10^{[A-B/(T+C)]} H_v \quad 5.2.1-7$$

A Gaussian profile is assumed for the laser as an approximation shown in Equation 5.2.1-7 where the Gaussian laser power is P_T , and r is the distance from the spot center. The laser flux is related to heat flux by the relation in 5.2.1-8:

$$|\bar{F}_L| = \frac{P_T}{2\pi\sigma^2} e^{-r^2/2\sigma^2} \quad 5.2.1-8$$

In the approximation where the spot is small compared to the asteroid, the laser flux can be re-calculated as shown in Equation 5.2.1-9:

$$F_L = \frac{-P_T}{2\pi\sigma^2} e^{-r^2/2\sigma^2} \hat{n} \quad 5.2.1-9$$

In the dynamic case, it is possible to solve for transient heat flow by Equation 5.2.1-10:

$$\nabla \cdot (K \nabla T) + \frac{d}{dT} (\rho c_v T) = 0 \rightarrow K \nabla^2 T + \rho c_v \frac{dT}{dt} = 0 \quad 5.2.1-10$$

In Equation 5.2.1-10, it is assumed that K (thermal conductivity) is independent of position, ρ and c_v are time independent. In the 2D steady state solutions, the thermal conductivity is assumed to be small (this is shown in 3D simulations to be a valid assumption as well as from first principle calculations) and a combination of radiation and mass ejection (phase change) is used as illustrated in Equation 5.2.1-11:

$$|F_L| = |F_{\text{rad}}| + |F_{\text{Ejecta}}| = F_T \rightarrow F_T = \sigma T^4 + M^{1/2} (2\pi RT)^{-1/2} 10^{[A-B/(T+C)]} H_v \quad 5.2.1-11$$

Inversion is not analytically tractable, so numerical inversion is used to get $T(F_T)$, which gives $P_v(F_T)$, $\Gamma_e(F_T)$, *etc.* In this inversion, a function fit is found (to 10th order typically), as shown in Equation 5.2.1-12:

$$T = \sum_{n=1}^N a_n (\log F_T)^n \quad 5.2.1-12$$

A Gaussian approximation to the laser profile is used (this is not critical) to get $T(r)$, $P_v(r)$, $\Gamma_e(r)$ where r is the distance from the center of the spot.

Since radiation goes as the 4th power of T , while the mass ejection from evaporation goes roughly exponentially in T , at low flux levels the outward flow is completely dominated by radiation (the asteroid is heated slightly and it radiates). As the spot flux level increases (spot size shrinks or power increases or both) evaporation becomes increasingly dominant and eventually at about $T \sim 2000-3000$ K or fluxes of 10^6-10^7 W/m² mass ejection by evaporation becomes the dominant outward power flow and (just as water boiling on a stove) the temperature stabilizes and increasing flux only increases the rate of mass ejection with only very small increases in temperature.

5.2.2 1D Energetics Simulations

Numerical implementations of the model are used to run simulations, both with phase-locked laser arrays as the illuminating source, and with phase-independent multi-beam configurations. Three methods are used for simulations

The heat of vaporization of a compound is the energy (*per mole or per kg*) to remove it from the bulk. Removal energy is related to an effective speed and an effective temperature, which are related to but somewhat different than the physical speed of ejection and the physical temperature of vaporization. To be more precise, the term evaporation refers to molecules or atoms escaping from the material (*for example water evaporating*), while boiling is the point at which the vapor pressure equals or exceeds the ambient pressure. At any non-zero temperature, there is a probability of escape from the surface: evaporation happens at all temperatures and hence vapor pressure is a quantitative measure of the rate of evaporation. The heat of vaporization is also temperature and pressure dependent to some extent. Table 5-2 gives thermal properties for various materials in asteroids. These materials have relatively high effective temperatures reflecting the fact that there is a probability distribution of energies and an increase in vapor pressure with respect to temperature (Lubin and Hughes, 2015).

Table 5-2. List of thermo-physical properties of common high temperature asteroid compounds. Here H_f is the heat of fusion and H_v is the heat of vaporization.

$v_{eff} = H_v^{1/2} [\text{J/kg}]$ and $T_{eff} = (M \cdot H_v) / 3R$ where $R = k N_A \sim 8.31$.

Material	H_f [kJ/mol]	H_v [kJ/mol]	M [g/mol]	H_v [10^6 J/kg]	C_v [J/kg-K]	V_{eff} [km/s]	T_{eff} [10^4 K]
SiO ₂	9.0	143	60.1	2.38	730	1.54	0.573
Al ₂ O ₃	14.2	293	102.0	2.87	930	1.69	1.15
MgO	77.4	331	40.3	8.21	1030	2.87	1.32
ZnS	38.0	320	97.5	2.46	472	1.57	1.28

The thermal probability distribution has tail areas allowing for escape from the surface at lower temperatures than one would naively conclude from a mean analysis only. If power P_T from the laser impinges on the asteroid in a small enough spot to heat to above the radiation dominated point (typically 2000-3000 K for rocky (monolithic) asteroids vs. 300-500 K for comets) it is possible to compute the evaporation flux (mass ejection rate) as: $M_e = P_T / H_v$. This is the maximum possible rate of mass ejection. It is possible to get quite close to this maximum if the system is designed properly.

5.2.3 2D Analytic Calculations

As mentioned above, this calculation assumes that the thermal conduction is small compared to radiation and mass ejection (a good assumption for most asteroids). Using the equations above and the numerical inversions it is possible to solve for the temperature distribution and thus the mass ejection and thrust on the asteroid among many other parameters. A summary is shown in Figure 5-7 for SiO₂. The parameter σ (sigma) in the Gaussian beam profile is allowed to vary to show the effects of non-ideal beam formation as well as beam and pointing jitter. As can be seen the system is quite tolerant to errors in beam formation, focus, beam jitter and pointing errors even beyond 10σ as long as the power is high enough. The requirements on a low power system at equivalent distances are more severe. These relationships also show that it is possible to nearly achieve the theoretical maximum mass ejection rate. Also, note the thrust (N) per watt

is close to 0.001 N/W for the 1000 kW case. This is comparable to the Shuttle SRB in thrust per watt. This is not really surprising, considering that conventional propellants are approximately thermal in nature with temperatures close to the maximum sustainable in the combustion chamber and exhaust nozzle (*i.e.*, a few $\times 10^3$ K). More conservative numbers are assumed for system performance, typically $80 \mu\text{N}/\text{W}_{\text{optical}}$ though calculations show the coupling to be between 100 and $500 \mu\text{N}/\text{W}_{\text{optical}}$ depending on the asteroid material composition and the laser flux on target used (Riley *et al.*, 2014). More laboratory measurements are needed for various materials and flux levels. For now, a conservative value of $80 \mu\text{N}/\text{W}_{\text{optical}}$ is assumed.

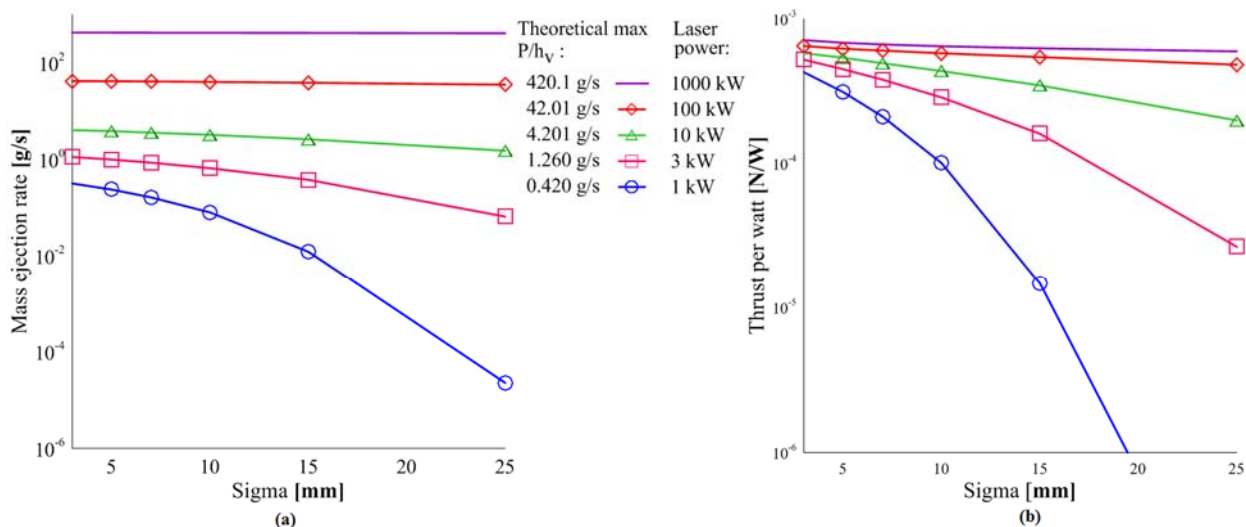


Figure 5-7: Using SiO₂ as the equivalent material. (a) Integrated mass ejection rates vs. sigma case for different powers between 1 kW and 1 MW. (b) Similarly, integrated thrust (N) per Watt vs. sigma. Lower power lasers, *i.e.*, under 10 kW, show significant performance reduction.

5.2.4 3D Numeric Calculations and Simulations

Thousands of 3D model simulations have been run, and a few salient results are apparent. Calculations based on the simplest assumptions, namely energetics, and the conservation of spot flux, were validated. The more sophisticated tools are needed for further analysis and optimization of the system. For the case of dynamic targeting and rotating objects, time evolution has been added to the 3D solver. Some of this is motivated by the need to understand the time evolution of the mass ejection under dynamic situations. This is partially shown in Figure 5-8, which illustrates the time evolution of the temperature at the center of the spot. Again, all cases refer to SiO₂ as the equivalent material for an asteroid. An orbiting system is modeled here with a 1 m laser array, with a Gaussian beam and a total optical power of 1 MW, and spot diameter ~30 mm ($\sigma \sim 5$ mm). SiO₂ is used as a reference material; simulations have also been run for 92 elements and a number of compounds relevant to asteroid composition, including olivine family and other ultramafic minerals. All simulations produce essentially similar results for most of the appropriate compounds, within a factor of a few (Lubin and Hughes, 2015). It is now possible to simulate full dynamics and apply this to the case of rotating asteroids. The same techniques can be applied to pointing jitter and laser machining (deliberate interior targeting) of the asteroid or other target.

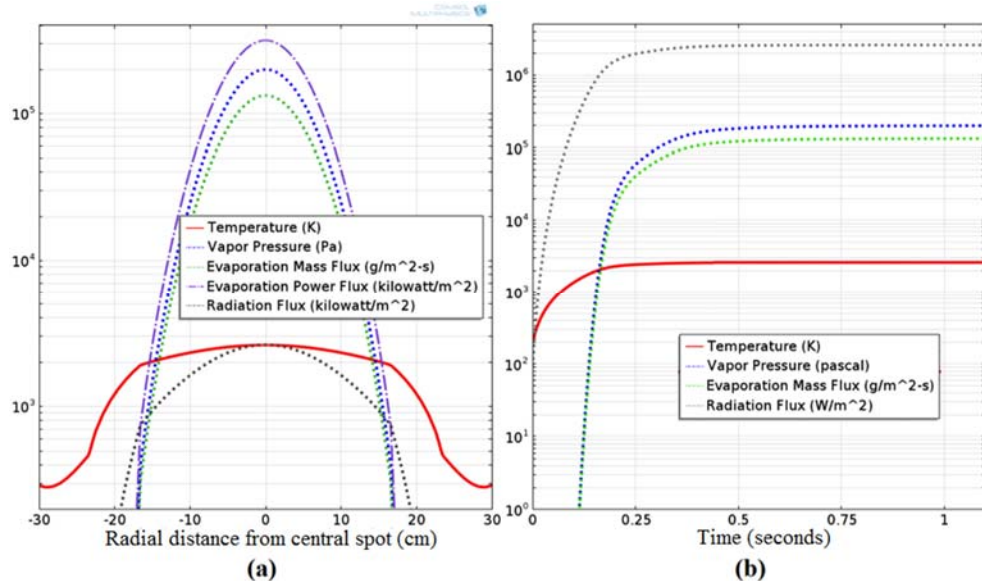


Figure 5-8: (a) Temperature, vapor pressure and mass loss distribution vs. distance from center (angle from beam axis). High frequency sub structure is due to numerical meshing. (b) Transient time solution (stationary) of temperature in the spot center (K) vs. Time (seconds) after the laser is turned on at $t=0$. Initial temperature is 200 K. Mass ejection begins within 1 second. This case is for a 1 m optical aperture and 1 MW of optical power with a spot diameter ~ 30 mm ($\sigma \sim 5$ mm) on the target which is approximately 15 km away from the spacecraft. The same spacecraft could be over 100 km away from the target and still have about the same deflection.

The model suggests that vaporization commences within ~ 1 second; the thermal profile stabilizes at a level consistent with the vaporization temperature of Silica in vacuum. Temperatures within the illuminated spot rise to the point of being mass ejection limited, which is ~ 2250 K in the center of the spot. The steady-state temperature stabilizes at a level consistent with the vaporization temperature of Silica in vacuum. Results of a simulated run are shown in Figure 5-9.

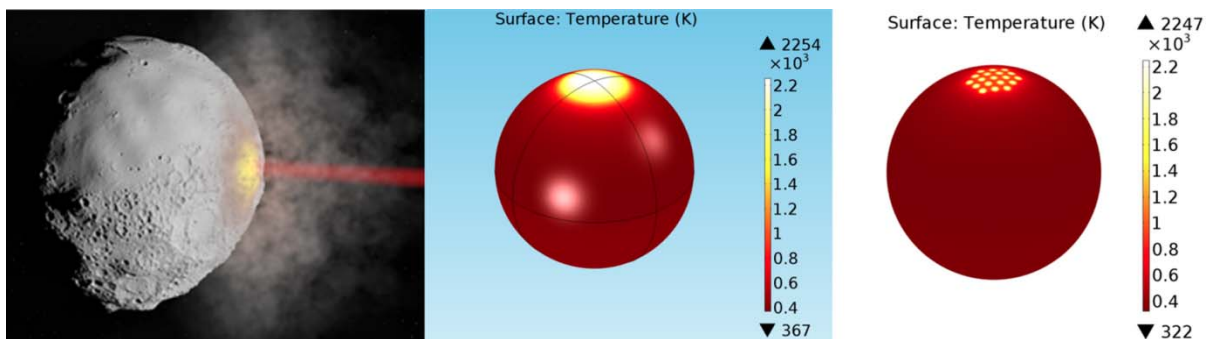


Figure 5-9: Results from a multi-physics model of a spherical bolide of microcrystalline Silica (SiO_2). Model features include radiation, conduction and mass ejection. Left: Conceptual illustration of a directed energy beam impinging on an asteroid; surface material is ejected from the heated spot, creating a plume. Center: Simulation results showing steady-state condition, under illumination with a single beam produced by an array of phase-locked lasers. Right: The same bolide, under

illumination with multi-beam emitter.

5.2.5 Comparison of Results among Thermal Simulations

While the 3D simulations give time transient solutions and include full thermal conduction, they lack the numerical flexibility of the 2D solutions. Results of the temperature distributions for a Gaussian laser illumination are compared, and found to be very close in their predictions. This builds confidence that it is possible to do both 2D and 3D simulations with high fidelity. Figure 5-10 shows comparisons of Gaussian beam illuminations; results are nearly identical in the critical central region. The ultimate test will come when comparing model results with laboratory tests. As laboratory tests are refined, the results will feed back into the models for various materials.

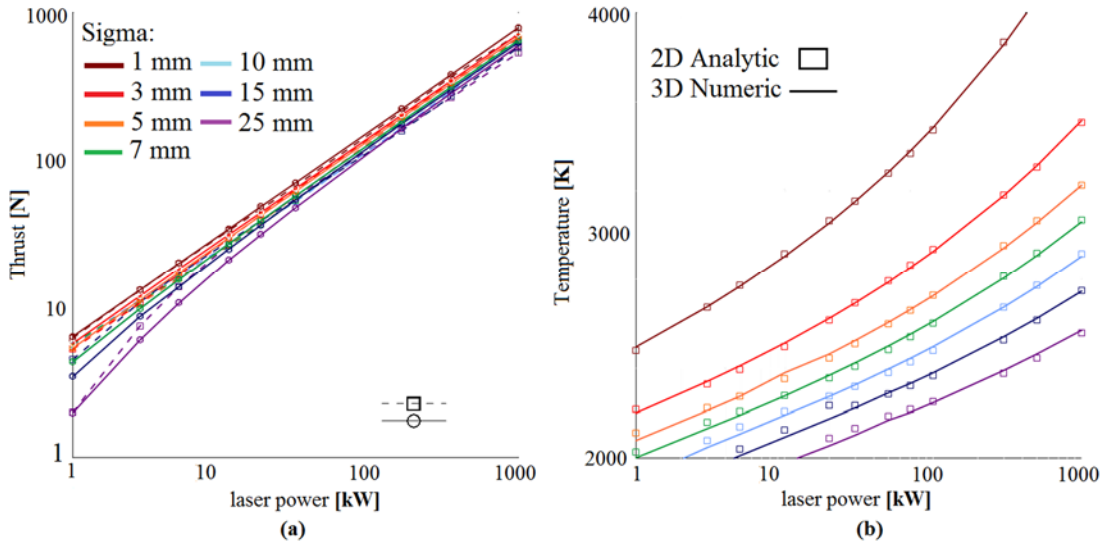


Figure 5-10: Comparison of 2- and 3-D models, hence numeric + analytic values for (a) integrated surface thrust (N) vs. total laser power for sigma between 1 and 25 mm. Note that the spot diameter ($\sim 6\sigma$) for a kW class system is typically 3 to 75 mm. (b) Central spot temperatures. (In this case: ~ 1 m aperture)

5.2.6 Asteroid Thermal Properties

Unfortunately it is not possible to bring asteroids into the laboratory to study their thermal properties, so it is necessary to rely on astronomical observations, primarily in the infrared, combined with assumptions about their formation and likely structure, to deduce their properties. Several references (Mueller, 2007; Mueller *et al.*, 2007; Harris, 1998; Delbò *et al.*, 2007; Margot *et al.*, 2002), among many others, have done excellent work in this area and it is possible to use their results. It is possible to derive the thermal properties by studying the time varying temperature as deduced from infrared observations. In this way the thermal inertia Γ ($\text{J/m}^2 \text{ K s}^{1/2}$) and thermal conductivity K [W/m K] are derived. The relationship between them is shown in Equation 5.2.6-1:

$$\Gamma = [\rho K C]^{1/2} \quad 5.2.6-1$$

Where:

ρ = Density [kg/m^3]

C = heat capacity [J/kg K]

Hence the thermal conductivity can be found by Equation 5.2.6-2:

$$K = \Gamma^2 / (\rho C) \quad 5.2.6-2$$

The data is shown in Figure 5-11 best fit to published data (Delbò *et al.*, 2007), where D is the asteroid diameter [km] is given in Equation 5.2.6-3:

$$\Gamma = d D^{-\xi} \quad 5.2.6-3$$

Substituting $d = 300$ [km], and $\xi = 0.4$, gives the relation for thermal conductivity in Equation 5.2.6-4:

$$K = 3e4 D^{-0.8} / (\rho C) \quad 5.2.6-4$$

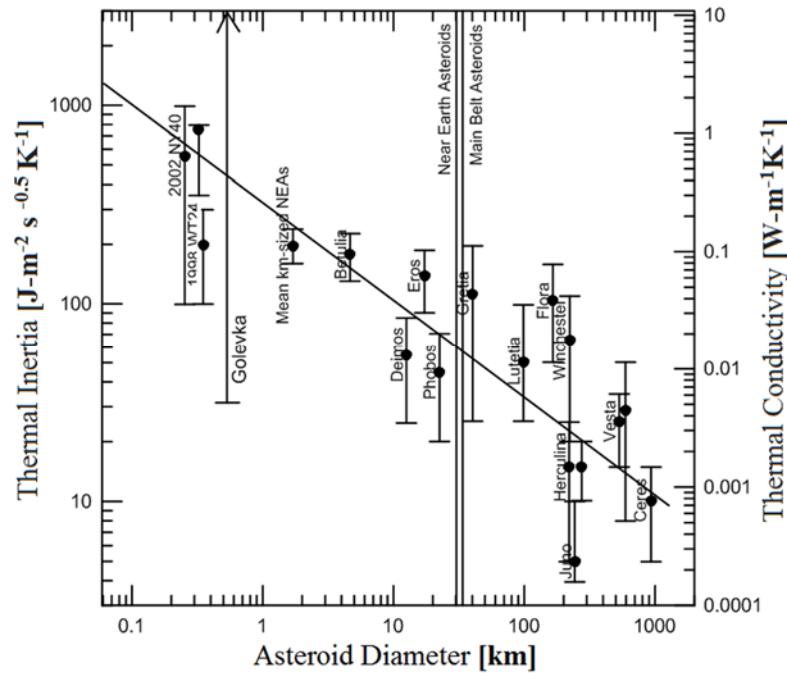


Figure 5-11: Thermal Inertia Γ [J/m² K s^{1/2}] and Thermal Conductivity: K [W/m K] plotted against asteroid diameter, showing a linear relationship that extends over diameters between 0.1 km through 1000 km.

The trend (*with some significant deviations*) is towards smaller asteroids having larger thermal conductivity and larger asteroids having smaller thermal conductivity. Some of this may be the point contacts from rubble-pile effect for larger asteroids. A similar trend between asteroid size and thermal inertia is also observed. It is the values that are of interest in the models. A relatively conservative case of $K = 1$ [W/m K] is assumed. To put this in perspective, some values for common materials are given in Table 5-3.

Table 5-3. Common material thermal properties for comparison to the asteroid thermal properties in Fig. 24

Material	K [W/m K]	ρ [kg/m ³]	C [J/kg K]	Γ [J/m ² K s ^{1/2}]
Nickel	91	8850	448	1.9×10^4
Iron	81	7860	452	1.7×10^4
Granite	2.9	2750	890	2600

Ice (solid)	2.3	917	2000	2040
SiO₂ (solid)	1.04 (at 200 °C)	2200	1000	1510
Water (liq 0°C)	0.56	1000	4200	1500
Snow (firm)	0.46	560	2100	740
Soil (sandy)	0.27	1650	800	600
Pumice	0.15	800	900 (varies significantly)	330
Styrofoam	0.03	50	1500	47
Air	0.026	1.2	1000	5.6
Moon (regolith)	0.0029	1400	640	51

Raising laser power from 10 kW to 20 kW resulted in slightly smaller range between minimum and maximum final temperatures with a relatively small effect on the final temperature between the two laser powers. This is to be expected since the effective vapor pressure and hence mass ejection rate and hence power into mass ejection is a strong function of the temperature. For these simulations, a relatively conservative case of $K = 1 \text{ W/m K}$ is assumed. For values of thermal conductivity between 0.01 and 250 W/m K, the evaporation mass flux and thrust change only slightly, shown in Figure 5-12.

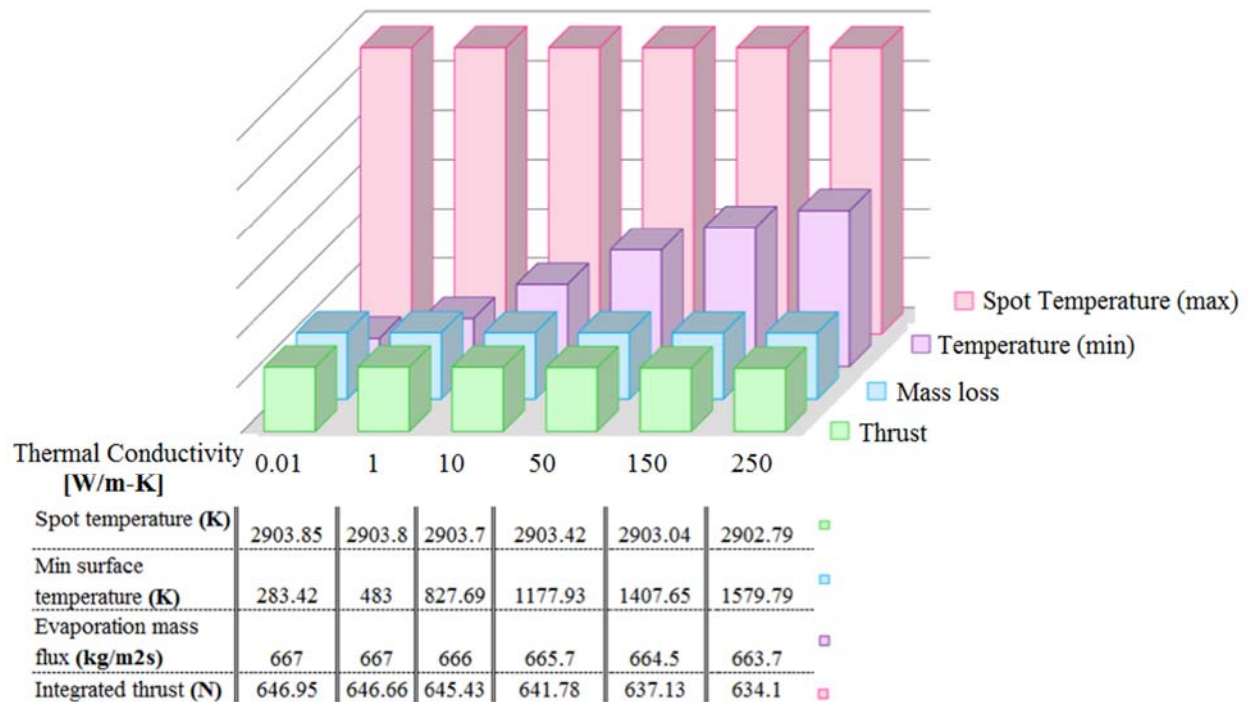


Figure 5-12: Extreme values inputs of thermal conductivity set to 0.01-250 W/m K for SiO₂ – Using 1 MW laser power, spot diameter is 60 mm, with sigma 10 mm, in this case for a 2 m diameter asteroid.

5.2.7 Effects of Rotation on Substrate Thermal Heating

All asteroids rotate, but generally quite slowly for larger one. A complete picture of rotation properties is not available, but from the limited data collected on the rotation of larger bodies and the break up speed it is estimated that asteroids in the 0.1-1 km class typically rotate no faster than once per several hours as seen in Figure 5-13. Results of detailed observation

indicate the rotation properties for more than 6000 significantly rotating asteroids and conclude that fast rotation is not an issue in general for larger asteroids (>150 m) as they are typically gravitational bound rubble piles (Walsh *et al.*, 2012) and for these the maximum rotation is independent of diameter and only depends on density ρ , with an angular speed ω , and rotation period τ given by:

$$\omega = \sqrt{\frac{4}{3} \pi G \rho} = \frac{2\pi}{\tau}, \tau = \sqrt{\frac{3\pi}{G\rho}} \quad 5.2.7-1$$

Where:

$$\tau \approx 1.19 \times 10^4 \rho[\text{g/cc}]^{-1/2} \text{ s} \approx 3.3 \rho^{-1/2} [\text{hr}], \text{ independent of diameter.}$$

Estimated densities are in the range of $\rho \sim 2$ [g/cc] yielding a minimum rotation period of about 2.3 hours. This is clearly seen in Figure 5-13.

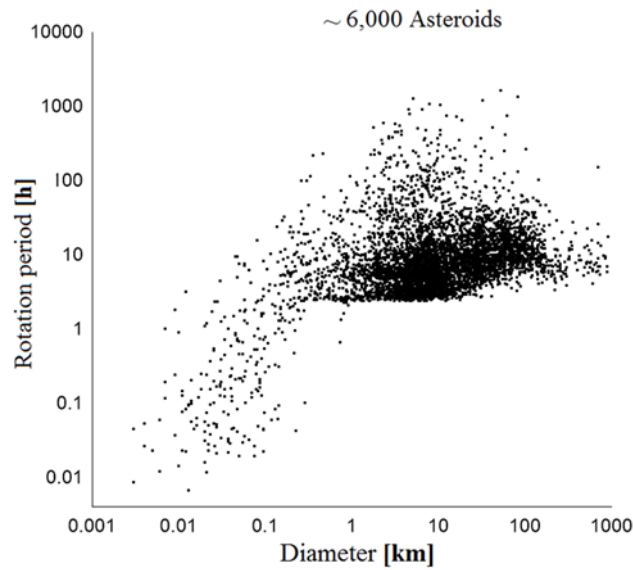


Figure 5-13: A distribution of measured rotation period of ~6000 asteroids. Notice the very sharp cutoff at just above ~2.2 hours for larger diameter asteroids. Data are from the Minor Planet Center (Harris, 1998). The superfaster rotators, those at the lower left with periods < 2.2 hours and $d < 0.1$ km are likely molecularly bound and form a distinct population. The bulk of the distribution, with diameters above 1 km and rotation periods above ~2.2 hours, may not be molecularly bound. Rotation periods above ~10 hours could allow rubble-pile accumulations of smaller bolides.

The cutoff in rotation periods is observed to be remarkably sharp, and lies very close to 2 hours for asteroids of diameters greater than approximately 150 m, consistent with equation 17. Some smaller asteroids can rotate faster as they can have a tighter binding than purely gravitational (such as an iron meteorite) but these are relatively rare.

Even fast rotating asteroids can be dealt with since the mass ejection begins so quickly after the laser is turned on. As is seen in the transient thermal simulations in Figure 5-8, the mass ejection begins within about 1 second. It is largely a flux issue so that for the same flux at any distance the mass ejection remains at this rate. This is assuming an asteroid consisting of solid

SiO₂, which is extremely conservative. Loss is included to mimic the absorption qualities of asteroids, which are very absorptive having typical reflection coefficients around 5-10%. Thus, a rotating asteroid with this rate (1 hour) poses little problem. More interesting perhaps would be an attempt to spin up (or down) an asteroid depending on beam placement as discussed below (Griswold *et al.*, 2015).

The time scale for mass ejection is also dependent on thermal conductivity, density, heat capacity and heat of vaporization. It is possible to make an estimate of the effects of asteroid rotation by considering the effective motion of the laser spot in the worst case of the spot on the equator. The spot will then move relative to the asteroid surface at a surface speed determined by both the rotation period and the diameter of the asteroid, illustrated in and Figure 5-15. One simple way to think about the relative time scales is to compare to mass ejection time (after laser initiation) to the time to move the laser spot by about one spot size. If the spot moves a large amount (compared to the spot size) in the time it takes to begin mass ejection then the system will be seriously compromised in terms of effectiveness. The bottom line is that faster rotating asteroid need higher power levels and slower can use lower power. A possible solution to reduce the average power is to use the laser in a pulsed (higher peak power) mode to de-spin it and then run CW to deflect it to optimize the lowest possible average power needed. The pulsed high peak power mode allows for higher flux so spot smearing effects are not as important and allows the target to be spun down to near zero rate relative to the velocity vector. Once the asteroid is spinning slowly enough the CW laser mode can start for full deflection capability. Simulation results are shown in Figure 5-14.

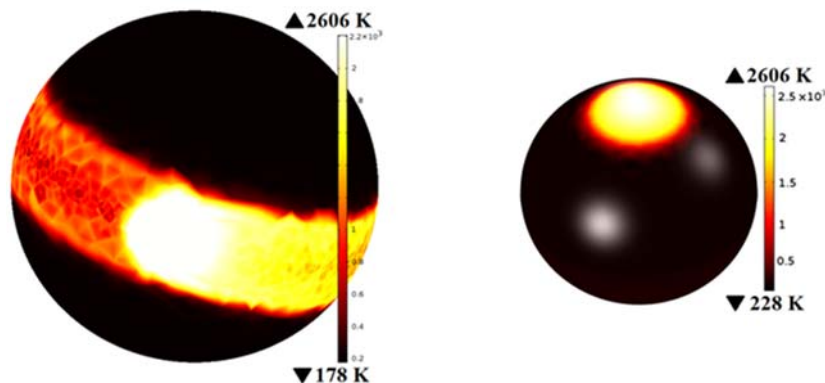


Figure 5-14: Rotating and stationary 3D plots for SiO₂: Using 1 hour rotation period for a 100 m diameter asteroid, yields equal surface temperature distribution as in the stationary steady state case. Temperatures rise to the point of being mass ejection limited, which is about 2600 K in the center of the spot. Solar illumination is modeled with an isotropic average of 350 W/m². The 1 hour rotation period is faster than the self-gravitating case and is shown as an extreme example of a large rotating asteroid that is not a rubble pile.

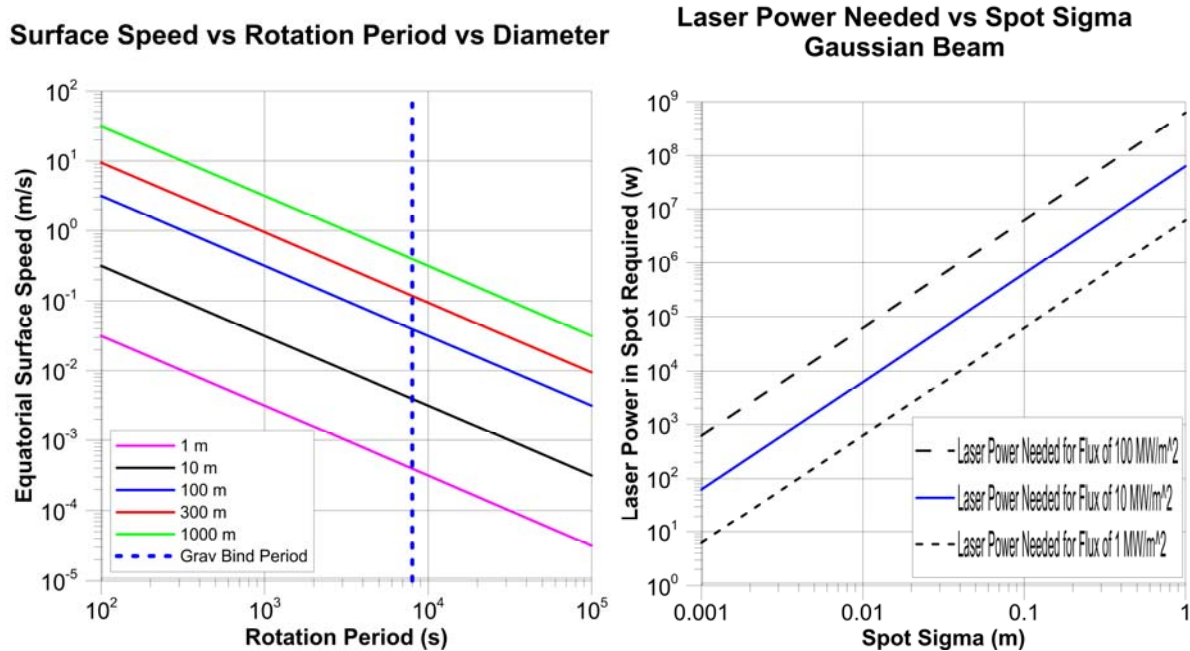


Figure 5-15: Left: Laser spot surface speed at the equator vs. rotation period vs. diameter of the asteroid. The 2.3 hour gravitational binding limit (rubble pile limit) is shown for reference for a density = 2 g/cc asteroid. Right: Laser power needed vs. the spot sigma for a Gaussian laser beam for three different flux level requirements. Typically 10 MW/m² is sufficient flux for most materials to be efficient at mass ejection. The effective spot diameter can be estimated as $\sim 6 \sigma$ depending on how one views a Gaussian beam to spot diameter conversion. The way to think about this is you want the surface speed (Left figure) to be less than one spot diameter per second (since the time to mass ejection is typically around 1 s or less). Knowing the spot speed you can then determine the laser power needed to reach the flux required (Right figure). This then drives you to larger power levels for larger diameter asteroid for the same rotation period. As an example to effectively work with a 100 m diameter asteroid that is a rubble pile (2.3 hour rotation rate) you have about a 5 cm/s spot speed. This then requires a spot sigma around 1-5 cm which requires a power level of about 10-60 kW. For a 300 m diameter asteroid rotating at the rubble limit you have a 12 cm/s spot speed and need a spot sigma of 2-10 cm with a power level of 30-700 kW. Slower rotating asteroids need less power and faster ones need more. Running the laser array in an optional pulsed high power mode (short duty cycle so average power remains the same) can overcome this problem allowing the asteroid to be de-spun first and then fully deflected while running in CW mode (Griswold *et al.* (2015)).

5.3 Evaporation of Target Material and Resulting Plume Density

The energy required to vaporize materials on the surface of an asteroid is determined by the heat of fusion and required increase in temperature to bring the surface material to the melting point from (assumed) initial low temperature starting point. Figure 5-16 shows the relationship between vapor pressure in Pascals (N/m²) versus Temperature, and versus target flux, for several compounds that are thought to be common in asteroids (Lubin *et al.*, 2016; Lubin *et al.*, 2015).

The typical energy per m^3 is on the order of 10^{10} J to vaporize most materials. At temperatures exceeding ~ 2250 K, which occurs at fluxes greater than ~ 10 MW/m^2 , the vapor pressures of all compounds are very high. That is, none of these materials remain solid, and mass ejection rates will be high. Even vapor pressures in the range of 10^3 Pa (0.01 atmospheres) correspond to large mass ejection rates.

The curves in Figure 5-16 are applicable to the worst case of complete chemical binding (*i.e.*, solid). In contrast to the small iron-rich meteorites that are sometimes found on the ground, a more typical asteroid likely has much lower thermal conductivity, for example in cases where the asteroid is an agglomeration of smaller fragments (a “rubble pile” asteroid). In many cases asteroids, will have significant amounts of low temperature volatile materials that lower the power requirements for evaporation of surface material. Asteroids are also molecular rather than atomic in species in general, but the conclusion are the same, namely at temperatures in the range of 2 000 to 3 000 K or target fluxes in the range 10^6 to 10^8 W/m^2 , all known materials will undergo vigorous evaporation. What is critical is to increase the spot flux to the point where evaporation becomes large. It is not sufficient to simply apply a large amount of total power, there has to be a large flux to initiate evaporation.

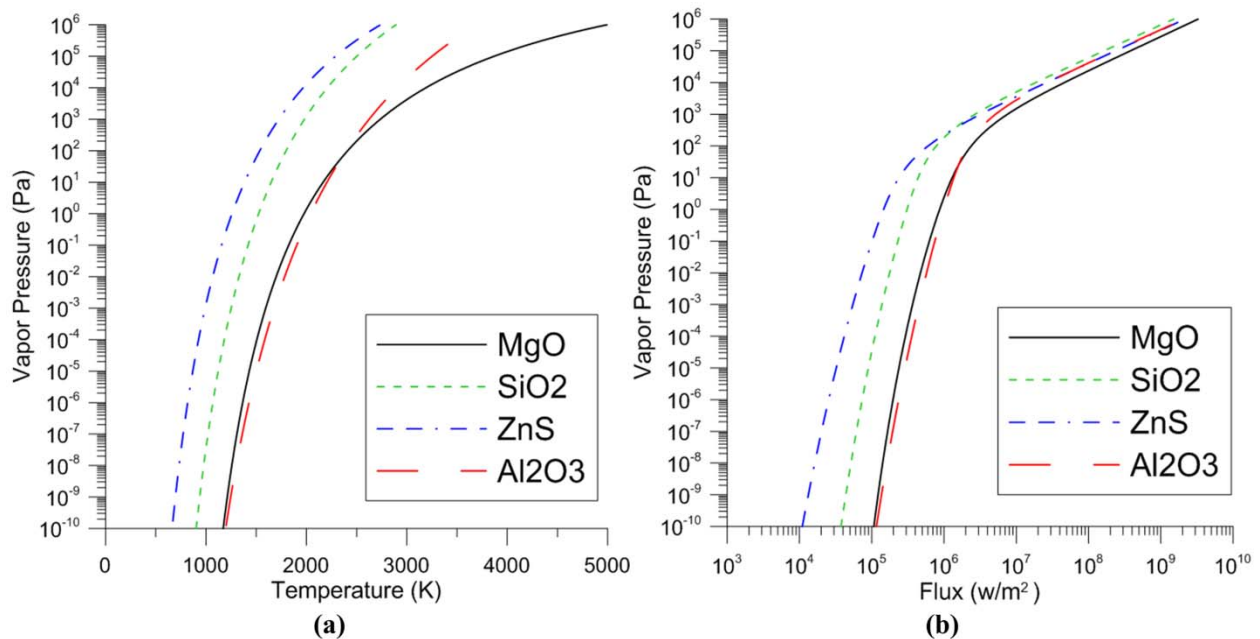


Figure 5-16: Vapor pressure relationship with temperature flux for several compounds that are thought to be common in asteroids (Lubin *et al.*, 2016; Lubin *et al.*, 2015). Left: Vapor pressure vs. Temperature for selected compounds. Right: Vapor pressure vs. target flux for the same compounds. Compounds include MgO, SiO₂, ZnS and Al₂O₃.

To calculate the mass ejection, use Langmuir’s equation for evaporation. The particle ejection rate, or evaporative flux, I_e (molecules $\text{m}^{-2} \text{s}^{-1}$) is given by Equation 5.3.0-1:

$$I_e = \frac{\alpha_e (P_v - P_h)}{\sqrt{2\pi m k T}} = \frac{\alpha_e N_A (P_v - P_h)}{\sqrt{2\pi M R T}} \quad 5.3.0-1$$

Symbols used in equations and text in this section are defined in Table 5-4. The mass flux Γ_e (kg m⁻² s⁻¹) is found from the Langmuir equation Equation 5.3.0-1:

$$\Gamma_e = I_e m = \frac{m \alpha_e (P_v - P_h)}{\sqrt{2\pi m k T}} = \frac{M \alpha_e (P_v - P_h)}{\sqrt{2\pi M R T}} = \alpha_e P_v \sqrt{\frac{M}{2\pi R T}} = \frac{\alpha_e P_v}{v_{AV} \pi / 2} = \frac{\alpha_e P_v}{v_e} \quad 5.3.0-2$$

Alternatively, Equation 5.3.0-2 can be re-written as Equation 5.3.0-3

$$\Gamma_e = \frac{M \alpha_e (P_v - P_h)}{\sqrt{2\pi M R T}} = M^{1/2} (2\pi R T)^{-1/2} \alpha_e (P_v - P_h) \quad 5.3.0-3$$

Assuming the ambient pressure (P_h) is zero in vacuum, the average molecular speed is given in Equation 5.3.0-4:

$$v_{AV} = \frac{8RT}{\sqrt{\pi M}} \quad 5.3.0-4$$

Here, the effective speed (v_e) is defined as in Equation 5.3.0-5:

$$v_e = \frac{\pi v_{AV}}{2} = \sqrt{\frac{2\pi R T}{M}} \quad 5.3.0-5$$

Substituting the expression 5.3.0-5 into Equation 5.3.0-2 gives Equation 5.3.0-6:

$$\Gamma_e v_e = \alpha_e P_v \quad 5.3.0-6$$

This is effectively like rocket thrust (dm/dt)· v_e except per unit area, so pressure is given by Equation 5.3.0-7:

$$P_v = \frac{\Gamma_e v_e}{\alpha_e} \quad 5.3.0-7$$

where the expression $\Gamma_e v_e$ is the plume pressure. Rearranging terms in Equation 5.3.0-7 gives Equation 5.3.0-8:

$$\frac{\Gamma_e v_e}{P_v} = \alpha_e \quad 5.3.0-8$$

Finally, the mass flux (in kg m⁻² s⁻¹) is given by Equation 5.3.0-9:

$$\Gamma_e = 0.138 \alpha_e \sqrt{\frac{M}{T}} (P_v - P_h) \quad 5.3.0-9$$

In constant temperature systems there is often a significant boundary layer, often referred to as a Knudsen layer. In the case presented here, the temperature increases to the point of equilibrium between radiation, mass ejection and thermal conduction (for the time dependent case). Boundary layer effects are thus different as there is a source of additional power (the directed energy beam) that increases the temperature until equilibrium is reached. In an extreme case a Knudsen layer could completely prevent mass ejection while for a directed energy system this cannot happen unless the temperature rises to the point of complete radiation balance. For flux levels near 10 MW/m² this would be greater than 6 000 K. Thus the boundary layer is greatly mitigated by the constant directed energy impinging on the target. A related effect would be the scattering and reflection at a boundary layer that would prevent the beam from reaching the surface. This latter effect tends to be quite small given the relatively low density of the plume. The coefficient of evaporation is another related surface effect which is different in the case of a directed energy system as the spot temperature will rise until the material is ejected. In the current analysis these effects are neglected, and future work will address this issue.

Table 5-4. Terms used in equations and text in Section 3.

Symbol	Interpretation	Units
I_e	Evaporative flux	Molecules m ⁻² s ⁻¹
P_v	Vapor pressure	Pa
P_h	Ambient pressure (= 0 in vacuum)	Pa
α_e	Coefficient of evaporation, $0 \leq \alpha_e \leq 1$	unitless
m	Mass of molecule	kg
k	Boltzmann constant	m ² kg s ⁻² K ⁻¹
$M = mN_A$	Molar mass	kg mol ⁻¹
$R = NA_k$	Constant, ≈ 8.31	unitless
Γ_e	Mass flux	kg m ⁻² s ⁻¹
T	Absolute temperature	K
$(T)_C$	Celsius temperature	°C
v_e	Effective molecular speed	m s ⁻¹
v_{AV}	Average molecular speed	m s ⁻¹
$(P)_T$	Pressure	Torr
$(P)_{Hg}$	Pressure	mm Hg
H_v	Heat of vaporization (or sublimation)	J kg ⁻¹
H_F	Heat of fusion	J kg ⁻¹
F_L	Laser flux	W m ⁻²
L_P	Laser Power	W
F_{rad}	Outgoing radiation flux	W m ⁻²
F_{ejecta}	Outgoing mass ejecta flux	W m ⁻²
F_{cond}	Ingoing conduction flux	W m ⁻²
$A, B \text{ and } C$	Antoine Coefficients for Compound	°C ⁻¹ , °C ⁻¹ and °C

The vapor pressure of each element or compound can be computed from its associated Antoine coefficients (A, B, C). Based on the computed vapor pressures, the mass ejection flux can be determined for the full 3D and 4D cases numerically. Note that in most cases, the Antoine coefficients are computed for Celsius temperature, and pressures are reported in mm Hg:

$$(P_v)_{Hg} = 10^{\left[\frac{A-B}{(T)_C - C} \right]} \quad 5.3.0-10$$

The mass ejection flux is computed as:

$$|\bar{F}_{Ejecta}| = \Gamma_e H_{eff} = M^{1/2} (2\pi RT)^{-1/2} \alpha_e 10^{[A-B/(T+C)]} H_{eff} \quad 5.3.0-11$$

$$|\bar{F}_L| = |\bar{F}_{rad}| + |\bar{F}_{Ejecta}| + |\bar{F}_{cond}| \quad 5.3.0-12$$

Assuming a Gaussian laser of power L_P , the (radial) laser flux is given by:

$$|\bar{F}_L| = \frac{L_P}{2\pi\sigma^2} e^{-r^2/2\sigma^2} \quad 5.3.0-13$$

where r is the distance from the spot center. In numerical solutions, the full 4D (time dependent) case is solved, using:

$$\bar{F}_L = \frac{-P_T}{2\pi\sigma^2} e^{-r^2/2\sigma^2} \hat{n} \quad 5.3.0-14$$

$$\bar{F}_{rad} = \sigma T^4 \hat{n} \quad 5.3.0-15$$

$$\bar{F}_{Ejecta} = \Gamma_e H_{eff} \hat{n} = M^{1/2} (2\pi RT)^{-1/2} \alpha_e 10^{[A-B/(T+C)]} H_{eff} \hat{n} \quad 5.3.0-16$$

5.4 Molecular Absorption of Radiation from the Heated Spot in the Ejected Plume

As a laser beam strikes the surface of a target, two important things happen. The surface is heated, creating a blackbody source; and, material is ejected from the surface into the surrounding space. A mass ejecta cloud forms in the space between the laser source and the target, providing an opportunity to observe the molecular absorption lines as the blackbody energy passes through the ejecta cloud. Typically, during evaporation or sublimation, the material coming off the target is not ionized and the spot temperatures are low enough that infrared vibrational and rotational lines are observed (Hill *et al.*, 2013; Barton *et al.*, 2013; Tennyson and Yurchenko, 2012). At the surface of the spot:

$$B(\lambda) (w / m^2 - m) = c\rho(\lambda) / 4 \quad 5.3.0-17$$

$$F(\lambda) (w / m^2 - st - m) = B(\lambda) / \pi = c\rho(\lambda) / 4\pi \quad 5.3.0-18$$

$$N(\lambda) (\gamma / m^2 - s - st - m) = F(\lambda) / h\nu \quad 5.3.0-19$$

where $F(\lambda)/h\nu$ is the photon flux at the surface of the spot. Symbols used in equations and text in this section are defined in Table 5-5. The ejecta density, in molecules per cubic meter, is given by:

$$n'(z, R) = \frac{4\Sigma}{v} [(1 - (R^2 / z^2 + 1)^{-1/2})] \quad 5.3.0-20$$

Where Σ is the ejecta flux, in molecules $m^{-2} s^{-1}$ from the spot. The ejecta flux can be determined as a number of particles:

$$\Sigma(\# m^2 s^{-1}) = \Gamma_e (kg(m^2 s^{-1}) / m) \quad 5.3.0-21$$

Note that the ejecta density at some distance z from the asteroid and a radial location R is given by:

$$n'(z, R) = \frac{4\Sigma'(z)}{v} = \frac{4\Sigma}{v} [1 - (R^2 / z^2 + 1)^{-1/2}] \quad 5.3.0-22$$

and that the following asymptotic relationships with distance hold:

$$n'(z, R) \rightarrow \frac{4\Sigma}{v} \text{ as } z \rightarrow 0, \quad \text{and} \quad n'(z, R) \rightarrow \frac{2\Sigma R^2}{v z^2} \text{ as } z \rightarrow \infty \quad 5.3.0-23$$

The integrated absorption line coefficient as a function of wavelength is found by:

$$\tau(\lambda) = \sigma(\lambda) \int_0^L n'(z, R) dz = \frac{4\Sigma\sigma(\lambda)}{v} \int_0^L [1 - (R^2 / z^2 + 1)^{-1/2}] dz \quad 5.3.0-24$$

Using the asymptotic relationships:

$$\int_0^L [1 - (R^2 / z^2)^{-1/2}] dz = L - (R^2 + L^2)^{1/2} + R \rightarrow R \text{ as } L \rightarrow \infty \quad 5.3.0-25$$

and:

$$\tau(\lambda) = \frac{4\Sigma\sigma(\lambda)}{\nu} R \text{ as } L \rightarrow \infty \quad 5.3.0-26$$

Table 5-5. Terms used in equations and text in Section 4.

Symbol	Interpretation	Units
$n'(z, R)$	Ejecta Density at distance z and radial location R	atoms m^{-3}
R	Spot radius on asteroid	m
λ	Wavelength	m
Σ	Ejecta flux	atoms $\text{m}^{-2} \text{s}^{-1}$
$\sigma(\lambda)$	Absorption cross section	$\text{m}^2 \text{atoms}^{-1}$
$H(\lambda)$	Observed photon flux at telescope	$\gamma \text{m}^{-2} \text{s}^{-1} \text{m}^{-1}$
$G(\lambda)$	Observed photon rate received per unit bandwidth by telescope	$\gamma \text{s}^{-1} \text{m}^{-1}$
$N(\lambda)$	Spectral radiance emitted at the spot	$\gamma \text{m}^{-2} \text{s}^{-1} \text{sr}^{-1} \text{m}^{-1}$
$B(\lambda)$	Power emitted at the spot	$\text{W m}^{-2} \text{s}^{-1}$
$\rho(\lambda)$	Spectral density at the spot	$\text{J m}^{-3} \text{m}^{-1}$
$F(\lambda)$		$\text{W m}^{-2} \text{sr}^{-1} \text{m}^{-1}$
A_{Spot}	Spot area of asteroid = $\pi \cdot R^2$	m^2
A_T	Telescope area	m^2
L	Distance to asteroid	m
Ω_T	Solid angle of telescope as viewed from asteroid = $A_T/(4 \cdot \pi \cdot L^2)$	sr
$\tau(\lambda)$	Integrated absorption line coefficient (optical depth)	
Γ_ε	Ejected mass flux (from Eq. (9))	$\text{kg m}^{-2} \text{s}^{-1}$
n_0	Surface spot density	atoms m^{-3}

Giving the observed photon rate received per unit bandwidth by telescope as:

$$G(\lambda) = \frac{A_{\text{spot}} A_T}{4\pi L^2} N(\lambda) e^{-\tau(\lambda)} = \frac{A_{\text{spot}} A_T}{4\pi L^2} N(\lambda) e^{-(4\Sigma\sigma(\lambda)R/\nu)} \quad 5.3.0-27$$

And the observed photon flux at the telescope as:

$$H(\lambda) = G(\lambda) / A_T = \frac{A_{\text{spot}}}{4\pi L^2} N(\lambda) e^{-(4\Sigma\sigma(\lambda)R/\nu)} \quad 5.3.0-28$$

The absorption coefficient as a function of wavelength $\tau(\lambda)$ is given by:

$$\tau(\lambda) = n\sigma(\lambda)X = \frac{4\Sigma\sigma(\lambda)}{\nu} R \quad 5.3.0-29$$

where n is an effective density and X is an effective length, the following relationships hold:

$$n = \frac{4\Sigma}{\nu} \text{ and } X = R \quad 5.3.0-30$$

These relationships are reasonable, since it follows that $\Sigma = n \cdot \nu/4$ which makes sense. The effective length $X = R$, which is just the spot radius, hence:

$$\tau(\lambda) = n\sigma(\lambda)R \quad 5.3.0-31$$

5.5 Spectroscopy by Observation of Radiated Energy through the Ejected Plume

Spectroscopy is possible whenever sufficient absorption occurs in the plume. Absorption depends on the plume density along the path from the heated spot to the spectrometer. To

determine absorption, first calculate the mass ejection using Langmuir's equation for evaporation. Then, use thermal-physical properties of materials in the plume to determine spectral absorption. This section provides details of the end-to-end absorption model, with terms described in Table 1.

Table 5-6. Terms used for absorption model.

Term	Interpretation	Units
I_e	Evaporative flux	Molecules $\text{m}^{-2} \text{s}^{-1}$
α_e	Evaporation Coef. $0 \leq \alpha_e \leq 1$	unitless
P_v	Vapor pressure	Pa
P_h	Ambient pressure	Pa
M	Molar mass ($M = m \cdot N_A$)	kg mol^{-1}
m	Mass of molecule	kg
k	Boltzmann constant	$\text{m}^2 \text{kg s}^{-2} \text{K}^{-1}$
R	Constant, $NA_k \approx 8.31$	unitless
Γ_e	Mass flux	$\text{kg m}^{-2} \text{s}^{-1}$
T	Absolute temperature	K
$(T)_C$	Celsius temperature	$^{\circ}\text{C}$
A, B, C	Antoine Coefficients	$^{\circ}\text{C}^{-1}, ^{\circ}\text{C}^{-1}, ^{\circ}\text{C}$
$F(\lambda)$	Photon flux	$\text{W m}^{-2} \text{sr}^{-1} \text{m}^{-1}$
λ	Wavelength	m
n'	Ejecta Density	atoms m^{-3}
z	Distance from the spot	m
R	Spot radius on asteroid	m
Σ	Ejecta flux	atoms $\text{m}^{-2} \text{s}^{-1}$
$H(\lambda)$	Observed photon flux	$\gamma \text{m}^{-2} \text{s}^{-1} \text{m}^{-1}$
$G(\lambda)$	Observed photon rate	$\gamma \text{s}^{-1} \text{m}^{-1}$
A_T	Telescope area	m^2
$\sigma(\lambda)$	Absorption cross section	$\text{m}^2 \text{atoms}^{-1}$
$N(\lambda)$	Spectral radiance emitted	$\gamma \text{m}^{-2} \text{s}^{-1} \text{sr}^{-1} \text{m}^{-1}$
A_{Spot}	Spot area on asteroid	m^2
L	Distance to asteroid	m
Ω_T	Solid angle of telescope	sr
$\tau(\lambda)$	Optical Depth	m^{-1}
n_0	Surface spot density	atoms m^{-3}
$\rho(\lambda)$	Spectral density	$\text{J m}^{-3} \text{m}^{-1}$

The ejecta density, in molecules per cubic meter, is given by:

$$n'(z, R) = \frac{4\Sigma}{v} [(1 - (R^2 / z^2 + 1)^{-1/2})] \quad 5.5.0-1$$

Where Σ is the ejecta flux, in molecules $\text{m}^{-2} \text{s}^{-1}$ from the spot. The observed photon rate received per unit bandwidth by the telescope $G(\lambda)$ in $\gamma \text{s}^{-1} \text{m}^{-1}$ is calculated from the observed photon flux at the telescope $H(\lambda)$ and the spot area of the asteroid: Let $\sigma(\lambda)$ be absorption cross section (in $\text{m}^2 \text{atom}^{-1}$). Then, $\tau(\lambda)$ is the integrated absorption line coefficient:

$$\tau(\lambda) = \sigma(\lambda) \int_0^L n'(z, R) dz = \frac{4\Sigma\sigma(\lambda)}{\nu} \int_0^L [1 - (R^2 / z^2 + 1)^{-1/2}] dz \quad 5.5.0-2$$

and the observed photon rate is:

$$\begin{aligned} G(\lambda) &= \frac{A_{spot} A_T}{4\pi L^2} N(\lambda) \exp[-\int_0^L n'(z, R) \sigma(\lambda) dz] \\ &= \frac{A_{spot} A_T}{4\pi L^2} N(\lambda) e^{-\tau(\lambda)} \end{aligned} \quad 5.5.0-3$$

It is now possible to compute the observed spectrum (rate received) $G(\lambda)$ ($\gamma \text{ s}^{-1} \text{ m}^{-1}$) and (flux received) $H(\lambda)$ ($\gamma \text{ m}^{-2} \text{ s}^{-1} \text{ m}^{-1}$) as measured by a spectrometer as follows:

$$H(\lambda) = \frac{G(\lambda)}{A_T}, \quad \Omega_T = \frac{A_T}{4\pi L^2} \quad 5.5.0-4$$

Assuming the heated spot is a blackbody with temperature T for simplicity, with spectral radiance of $N_\lambda = N(\lambda)$ emitted at the spot, then the spectral density at the spot is:

$$\rho(\lambda) = \frac{8\pi hc}{\lambda^5 \cdot (e^{hc/\lambda kT} - 1)} \quad 5.5.0-5$$

It is now possible to calculate the observed spectra $G(\lambda)$:

$$G_\lambda = N(\lambda) A \Omega_T e^{-\tau(\lambda)} \quad 5.5.0-6$$

where the optical depth and surface spot density are:

$$\tau(\lambda) = 4\Sigma\sigma(\lambda)R / \nu = n_0\sigma(\lambda)R \quad 5.5.0-7$$

$$n_0 = 4\Sigma / \nu \quad 5.5.0-7$$

The calculated cross sections for four important molecular species, water silica, methane and titanium oxide, are shown as examples in Figure 5-17 and Figure 5-18.

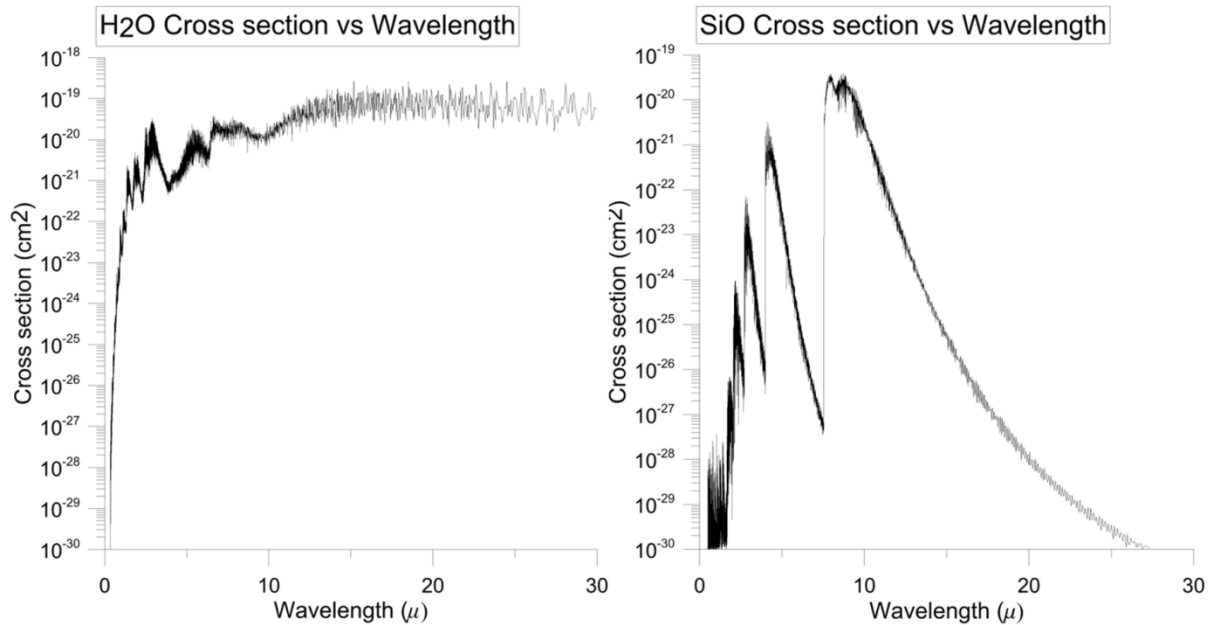


Figure 5-17: Calculated cross section vs. wavelength for water and silica. Molecular cross sections are given in cm^2 , over a range of wavelengths from $1\ \mu\text{m}$ through $30\ \mu\text{m}$. The cross-section pattern is distinct for each material, and provides diagnostic features for spectral composition analysis.

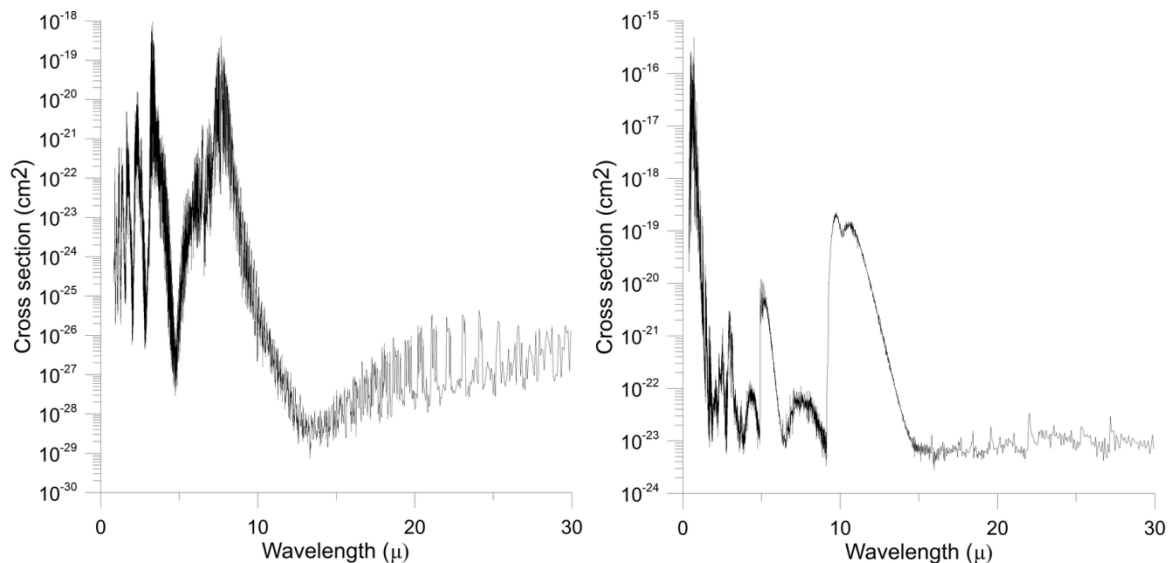


Figure 5-18: Calculated cross section vs. wavelength for methane, and for titanium oxide. Molecular cross sections are given in cm^2 , over a range of wavelengths from $1\ \mu\text{m}$ through $30\ \mu\text{m}$. The cross-section pattern is distinct for each material, and provides diagnostic features for spectral composition analysis.

5.6 Simulations of Absorption Spectra

Molecular cross sections for various compounds have been determined, for example from theory as described in Section 5.5. Theoretical cross sections can be used to predict absorption spectra under various operational scenarios. In a ‘stand-on’ scenario, a spacecraft could be equipped with a laser and a telescope/spectrometer. The spectrum observed by the spectrometer will depend on laser power and total aperture, the distance between the laser and the target, and the effective spot size on the target (and, of course, the molecular composition of the target). The end-to-end model was used to simulate a ‘stand-on’ mission with a 100 W laser with a 10 cm mirror. The spacecraft was positioned 100 m from a water-bearing bolide, producing a 1 mm effective spot size on the bolide. Results of the simulation are shown in Figure 5-19.

The simulated spectrum shown in Figure 5-19 will vary, depending on the concentration of water in the target. Figure 5-19 also shows results of several simulations using a 10 kW laser with a 10 cm mirror, positioned 1 km from the target, producing a 20 cm effective spot size on the bolide. The ice concentration in the bolide was varied from 0.1% to 100%. Based on the simulated spectra, water should be easily detected even at significant distances, given suitable laser and spectrometer equipment. The thermophysical properties of water contribute to the ease of remote detection. However, many rocky materials have more complex thermophysical properties, which can increase the difficulty of remote detection. Figure 5-20 shows results of a ‘stand-on’ mission to a titanium-oxide bearing target, using a 10 kW laser with a 10 cm mirror, positioned 100 m from the target, producing a 1 mm effective spot size on the bolide.

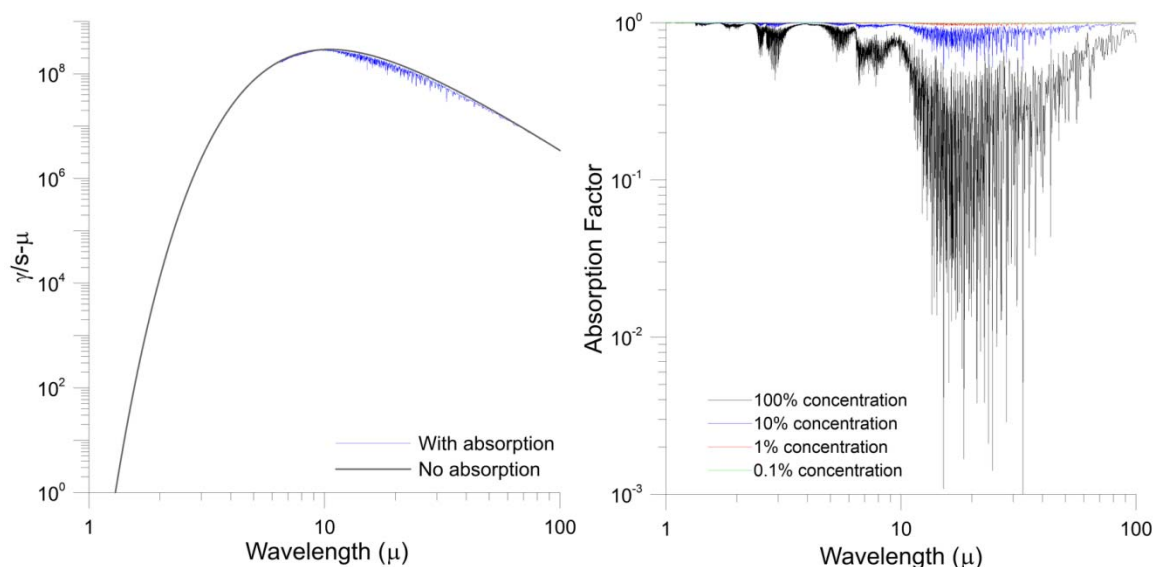


Figure 5-19: Simulated spectrum for a water-bearing bolide, as observed from a distance of 100 m. The simulation used a 100 W laser with a 10 cm mirror, producing a 1 mm diameter spot on the bolide. Simulated absorption factor (compared to no absorption of a water-bearing bolide with various concentrations of water, as observed from a distance of 1 km. The simulation used a 10 kW laser with a 1 m mirror, producing a 20 cm spot on the bolide.

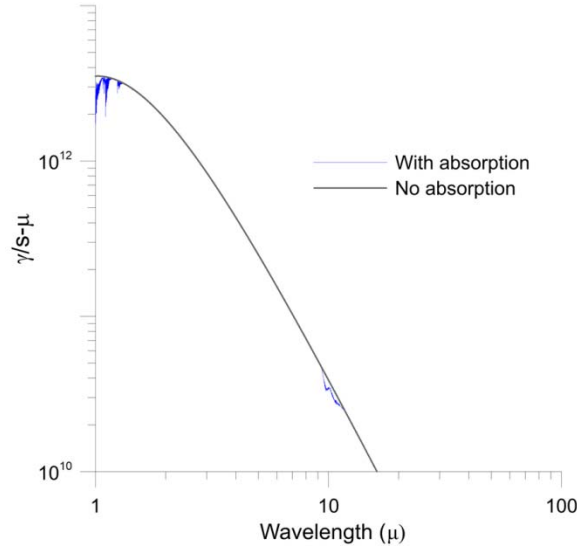


Figure 5-20: Simulated spectrum for a titanium oxide-bearing bolide, as observed from a distance of 100 m. The simulation used a 10 kW laser with a 10 cm mirror, producing a 1 mm diameter spot on the bolide.

5.7 Analysis of Extended Mission Capability

As discussed in Section 1.2, the laser system at the core of R-LEMA can be exploited for additional mission capabilities. This section explores several extended capabilities of R-LEMA, including a technical analysis of operational principles.

5.7.1 Orbital Deflection of Threatening Asteroids

Here a comparison is made between using an impactor (ramming asteroid) vs. using a laser. The launch mass is used as a common element for both cases—i.e., for the same launch mass, what can each system do? For a simplistic analysis the impactor delivers a large impulse or momentum transfer to deflect the target (integrated force - time in units of Ns). This momentum transfer imparts a change in the speed ΔV of the asteroid equals $\Delta p_{\text{impactor}} / M$ where M is the mass of the asteroid. $\Delta p_{\text{impactor}}$ is the impulse delivered at a time τ before (if un-deflected) impact.

$\Delta p_{\text{impactor}} = \beta \cdot m v$ where m is the spacecraft mass, v is the relative closing speed between the spacecraft and asteroid and β is an enhancement factor due to asteroid mass ejection from the impact. The enhancement factor is a much debated term that is a complex function of asteroid material properties at the impact site, geometry of impact, speed of impact. In general one assumes pure inelastic collision ($\beta = 1$) to be conservative as any *a priori* β is generally not going to be known for a given target. The assumption is that $\beta = 1$ but it is important to keep this enhancement possibility in mind to be fair. The change of speed is thus:

$$\Delta V = \beta m v / M = \beta v (m/M) \quad 5.7.1-1$$

Note that the deflection $\Delta x_{\text{impactor}}$ is linearly proportional to the spacecraft or impactor mass (m), the closing speed (v) and time to impact τ and inversely proportional to the asteroid mass M . Note that the asteroid mass M is proportional to the cube of the asteroid diameter D . The momentum change (impulse delivered) is largely independent of the asteroid mass and only depends on the spacecraft mass (m) and the closing speed (v). For a homogeneous asteroid of density ρ then deflection is:

$$\Delta x_{\text{impactor}} = 3 \Delta V \tau_{\text{impact}} = 18 m v \tau / (\pi \rho D^3) \quad 5.7.1-2$$

Since the asteroid is moving rapidly with typical speeds of 5-40 km/s it is possible to simplify this to assume the spacecraft is simply in the way of the asteroid (inelastic billiard ball) and thus the speed of the spacecraft relative to the earth is of lesser importance. This of course depends on the specifics of the asteroid orbit (closing from the front vs. the back of the asteroid orbit). Essentially then it is the mass of the spacecraft that is critical to maximize. Once the space craft is launched to LEO it is assumed that ion engines will be used to allow a larger fraction of the launch mass to survive until impact to maximize the impulse. Since the deflection is proportional to the inverse cube of the asteroid diameter, and the spacecraft mass is limited by the launcher capability, the only free parameter is the time to impact τ . In other words, the deflection is proportional to:

$$\Delta x_{\text{impactor}} \sim m v \tau D^{-3} \quad 5.7.1-3$$

For the case of directed energy, the *approximate* deflection using methods from Chesley and Chodas (2002) is:

$$\begin{aligned} \Delta x_{\text{laser}} &= 3/2 a \tau_{\text{laser}}^2 = 3/2 (a \tau) \tau_{\text{laser}} = 3/2 \Delta V \tau_{\text{laser}} = 3/2 (F/M) \tau_{\text{laser}}^2 \\ &= 3/2 F \tau_{\text{laser}}^2 / M = 3/2 \Delta p_{\text{laser}} \tau_{\text{laser}} / M = 9 \alpha P \varepsilon \tau_{\text{laser}}^2 / (\pi \rho D^3) \end{aligned} \quad 5.7.1-4$$

where:

a = acceleration imparted due to the laser plume thrust

F = laser plume thrust = $\alpha P \varepsilon$

P = laser power

α = laser plume thrust coupling coefficient – thrust per optical watt

ε = beam efficiency factor – fraction of beam that is in central spot

ρ = asteroid density

D = asteroid diameter

M = asteroid mass = $\pi \rho D^3/6$

τ_{laser} = laser ablation time (laser on time) – assumed to be on the entire time before impact and after rendezvous

$\Delta p_{\text{laser}} = F \tau_{\text{laser}} = \alpha P \varepsilon \tau_{\text{laser}}$

Note that the laser deflection Δx_{laser} is proportional to τ_{laser}^2 while the impact deflection is proportional to τ_{impact} . This is important as the deflection grows quadratically with time for the laser and linearly with time for the impactor. The laser thrust is assumed to be constant and the asteroid mass changes very little due to the mass loss from ablation and that the laser plume thrust is proportional to the laser power. For simplicity, the value $\alpha \sim 80 \mu\text{N/W}_{\text{optical}}$ is used, based on conservative laboratory measurements (Brashears *et al.*, 2015). These estimates are consistent with other published results (Gibbings *et al.*, 2013; Vasile *et al.*, 2014). Note that for the case of directed energy or any constant force (such as ion engines, gravity tractors, *etc.*) the deflection is:

$$\Delta x_{\text{laser}} = 3/2 \tau_{\text{laser}} \Delta p_{\text{laser}} / M \quad 5.7.1-5$$

Where while for the impulse delivery (effectively instantaneously at a time τ_{impact} before impact) for the same overall delta momentum delivered to the asteroid is:

$$\Delta x_{\text{impactor}} = 3 \tau_{\text{impact}} \Delta p_{\text{impactor}} / M, \text{ or: } \Delta x_{\text{laser}} = 1/2 \Delta x_{\text{impactor}} \quad 5.7.1-6$$

for the same Δp and τ , based on the approximation of Chesley and Chodas (2002). The question now becomes, “For a given launch mass which is more effective – impactor or laser?” If the deflection is set to be the same $\Delta x_{\text{impactor}} = \Delta x_{\text{laser}}$, then it is possible to compare the laser-on time to impact-time, both before nominal Earth impact:

$$\Delta x_{\text{laser}} = 3/2 \tau_{\text{laser}} \Delta p_{\text{laser}} / M = \Delta x_{\text{impactor}} = 3 \tau_{\text{impact}} \Delta p_{\text{impactor}} / M \quad 5.7.1-7$$

which gives:

$$\tau_{\text{impact}} / \tau_{\text{laser}} = 1/2 \Delta p_{\text{laser}} / \Delta p_{\text{impactor}} = 1/2 \alpha P \varepsilon \tau_{\text{laser}} / \beta m v \quad 5.7.1-8$$

Or

$$\tau_{\text{impact}} = 1/2 \alpha P \varepsilon \tau_{\text{laser}}^2 / \beta m v \quad 5.7.1-9$$

Note that the ratios of times $\tau_{\text{impact}} / \tau_{\text{laser}}$ grows linearly with τ_{laser} so that the time ratio depends on the specifics of the case and not just on the fixed system parameters $\alpha, P, \varepsilon, \beta, m, v$. The real situation is far more complex than the approximations used in Chesley and Chodas (2002), and anticipated results depend on the specifics of the asteroid orbit and mission parameters. An SLS Block 1 launch of 70000 kg to LEO is assumed. For high Isp ion engines of 3000 s (Hall effect thrusters baselined for ARM) or 6000 s (gridded ion) a large fraction of the LEO mass will make it to the asteroid. It can be shown that for the same mass limited launch the laser ablation system takes much less time to deflect the asteroid. This is a critical point: the conclusion here is that for the same launch mass, it would be possible to launch a 1-2 MW laser system and for many scenarios that will be far more effective than an impactor of the same mass.

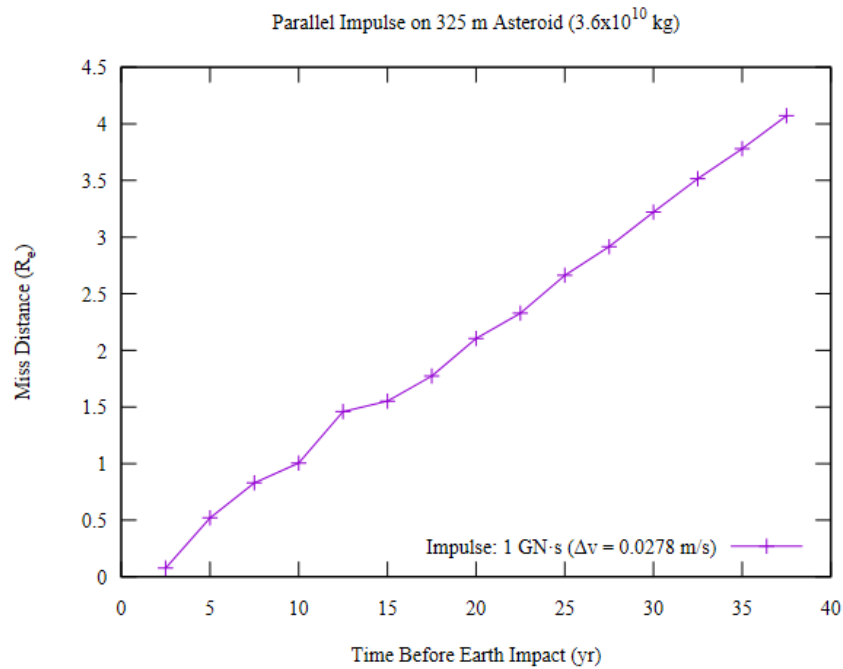


Figure 5-21: Deflection vs. impulse delivery time before impact for 1 GN s impulse using an impactor on an Apophis class asteroid (325 m diameter) using detailed numerical simulations (Zhang *et al.*, 2015-1; Zhang *et al.*, 2015-2; Zhang *et al.*, 2016). This impactor mass is somewhat larger than an SLS Block 1 can deliver. A deflection of 2 Earth radii (typ. min acceptable) would require interdiction about 10 years before impact using this impactor. The seemingly unusual behavior of deflection vs. time of impactor hit is due to resonance effects from the multiple orbits.

The details of the particular orbits are important but it is possible to draw some basic conclusions. Assuming 60000 kg makes it out to the asteroid and with a closing speed of 10 km/s, the impactor impulse is 6×10^8 Ns. Figure 5-21 shows that for this same 70000 kg SLS Block 1 to LEO, it would be possible to launch a 1 MW optical power laser delivering ~60 N of thrust on the

asteroid for an assumed laser coupling coefficient $\alpha \sim 80 \mu\text{N/W}$ optical with an assumed beam efficiency in the central spot of 0.7. To get the same deflection in the same time to impact as the impactor, the laser system needs to deliver twice the momentum as the impactor since the impactor delivers the momentum change essentially instantaneously while the laser delivers it slowly over the entire time the laser is on. Hence, the requirement is $1.2 \times 10^9 \text{ N s}$. At 60 N of laser plume thrust this would require a time $\tau = 1.2 \times 10^9 \text{ N s} / 60 \text{ N} = 2 \times 10^7 \text{ s}$ or about 7 months of laser exposure vs. using the same mass impactor which requires 10 years preemptive hit before Earth impact to obtain the same 2 Earth radii miss. This time ratio depends on the specifics of the asteroid orbit. Other differences for real systems are that typical impactor missions need more than one to make sure the impulse was delivered properly and that the asteroid orbital control with an impactor can be quite uncertain. For any real threat, multiple backups would be prudent.

5.7.2 Active Illumination for Threatening Asteroid Discovery

Continued discovery of NEOs, both large and small, is essential for protecting Earth from future impacts. The development of ground-based optical observatory networks and Earth-orbiting spacecraft with infrared sensors has increased the rate of discovery, but detection remains a difficult task. A large problem is that NEOs spend much of their orbit in the direction of the Sun when viewed from Earth, blinding current systems and leaving a large part of the sky unresolved. Another issue that current systems are facing is that the low emissivity of some objects makes detection by passive sensors difficult. Generally, asteroids are found by using their reflected sunlight and then looking for them in the visible bands or looking for them in their thermal IR using their heat signature. An orbiting laser phased array directed energy system could be used for active illumination of NEOs (Riley *et al.*, 2014). The baseline design consists of laser fiber amplifiers, which emit very narrow-band energy beams, to enhance discovery for much smaller and lower emissivity objects with a greater increase in range. This general technique is sometimes referred to as Light Detection and Ranging (LIDAR). Narrow bandwidth and precision beam control would aid in ephemeris refinement and Doppler velocity determination of objects already identified with wide-field surveys.

One of the difficulties with asteroid mitigation in general is knowing where the targets are. Generally, asteroids are found by looking for them in the visible bands using their reflected sunlight or in the thermal IR using their thermal IR signature. It is possible to use a laser system for active illumination of targets to aid in both their detection and orbital refinement. This is done in much the same way that a radar system works except with a laser the beams are much smaller, providing finer target determination and much greater range. The same phased array optical system is used for reception of the return light as is used for transmission of the laser. In this case, the system is run in a gated or long term pulsed mode. The light travel time to 1 AU is about 8 minutes or a round trip light travel time of 16 minutes. The laser could be turned on to scan potential targets and then turned off just before the photons that are scattered off the target are expected to return and switch to a receive mode. This then forms a complete LIDAR system with the same optics used for transmitting and receiving. The receive system could also be phased to form a full phased array receiver or could be run in a mode where each element acts as an independent receiver with the sum of all sub elements co-added before detection. There are advantages to this latter mode in both simplicity of operation and in that a much larger field of view is received eliminating scanning the field for reception. The disadvantage is the increased background from a larger field of view per sub element.

The return signal is computed for a variety of mission scenarios, as well as the equivalent mapping times for small error boxes to full sky blind surveys. The relevant backgrounds are the Cosmic Infrared Background (CIB), the Zodiacal background, and the asteroid's scattered sunlight and thermal emission. This technique not only allows for an "in situ" and "co-aligned" determination of the target position, but also gives ranging from time of flight (or phase modulation) as well as speed from measured Doppler. Here a heterodyne technique is assumed for detection, which is now feasible at the baseline wavelength. This is another relatively new development in photonic technology.

5.7.3 Laser-Beamed Spacecraft Propulsion, Power and Communications

Scientists and the public have long been interested and fascinated with methods for relativistic travel to allow interstellar and intergalactic travel. A few of the projects that have studied it are Project Orion, a nuclear pulse propulsion spacecraft studied in the early 1950s (Bussard, 1958); Project Daedalus, a two-stage spacecraft utilizing fusion rockets capable of traveling 6 light years in 50 years (Bond and Martin, 1978); and Project Longshot, a US Naval Academy and NASA proposed nuclear fission spacecraft (Beals *et al.*, 1988). While these areas of thought have been around for decades, current capabilities in space travel are meager at best compared to our dreams. For example, the maximum spacecraft speed obtained to date is by the Voyager 1 spacecraft, at about 17 km/s (relative to the sun) and while new technologies such as ion engines promise more efficient use of propellant, no current technologies are practical for travel to even the nearest stars in a human lifetime.

Using a laser as a photon drive is not a new idea. For example, Marx (1966) proposed an Interstellar vehicle propelled by terrestrial laser beam. R.L. Forward (1983, 1984) proposed a solar pumped laser. Forward proposed using a 1000 km diameter Fresnel lens to focus the laser on a spacecraft composed of a 1000 kg mirror system. What is new is that recent and very rapid developments with photonics allow new laser technologies capable of very high efficiency and the ability to phase lock to synthesize a narrow beam. Modern systems based on laser arrays have been proposed for interplanetary missions (Lubin *et al.*, 2015; Bible *et al.*, 2013).

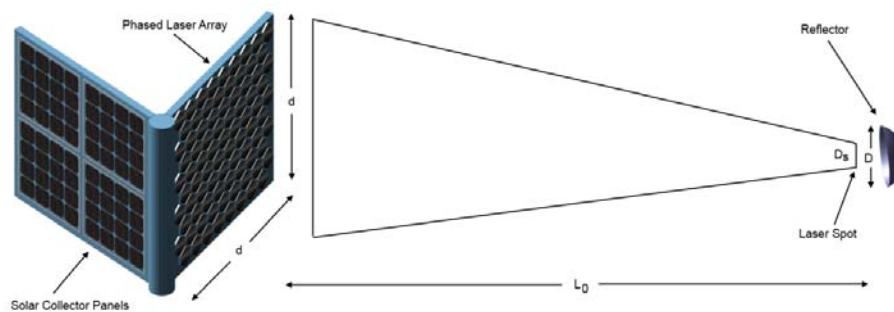


Figure 5-22: Diagram depicting relevant variables. L is the distance to the spacecraft and L_0 denotes the distance of the spacecraft when the beam spot equals the reflector size. As the spacecraft moves outward, the laser spot size (D_s) increases in proportion to the distance L to the spacecraft and ultimately, D_s becomes larger than D at which point the photon force begins to decrease proportional to the ratio of the spot to reflector area or $(D_s/D)^2$.

Another use of the laser system would be for long range interstellar communications to and from an interstellar spacecraft. This is a critical issue for long range interstellar probes in the future. Can we get high speed data back? Consider an optical link calculation at a distance of $L = 1$ ly ($\sim 10^{16}$ m) the spot size (diameter) is about $D_s \sim 2 \cdot 10^6$ m. For the case of the 100 kg robotic craft and with a 30 m diameter reflector this gives a spacecraft received photon rate of $3 \cdot 10^{29} \times (30/2 \cdot 10^6)^2 \sim 7 \cdot 10^{19}$ γ /s. Assuming it takes 40 photons per bit (which is very conservative) this yields data rate of about $2 \cdot 10^{18}$ bits/s, clearly an enormous rate. Assume the spacecraft has a very modest 10 W transmitter on the spacecraft (an RTG for example) for an optical link at the same basic wavelength ~ 1.06 μ m (slightly different to allow full duplex communications if needed) and that it uses the same 30 m reflector as for the photon drive but this time it uses it as the communications transmitter antenna (mirror). At a distance of $L = 1$ ly ($\sim 10^{16}$ m) the spot size (diameter) is about $D_s \sim 3.5 \cdot 10^8$ m. For the case of the 100 kg robotic craft and with a 30 m diameter reflector transmitting back to a receiving array gives a received photon rate of $5 \cdot 10^{19} \times (10^4/3.5 \cdot 10^8)^2 \sim 4 \cdot 10^{10}$ γ /s. Assuming it takes the same 40 photons per bit this yields a received (at Earth or wherever the receive system is located) data rate of about $1 \cdot 10^9$ bits/s or 1 Gbps. At the nearest star (Proxima Centauri) at a distance of about 4 ly the data rate at Earth from the spacecraft is about 70 Mbps. Live streaming >HD video looks feasible all the way to our nearby interstellar neighbors, with suitable equipment (Lubin *et al.*, 2015; Bible *et al.*, 2013).

6. TECHNICAL GOALS AND CHALLENGES BEYOND PHASE I

6.1 Experimental Approach for Elevating System Readiness

The system concept could be elevated from TRL-2 to TRL-4, by building a proof-of-concept laboratory model and running extensive experiments to test the theory developed in Phase I. In particular, Phase I results suggests that the heated spot will produce sufficient blackbody flux to be viewed from a distance, so that flux is not the limiting component of the system. Phase I results also indicate that much of the absorption occurs within about one spot radius from the target. Thus, spectral detection is limited primarily by ejecta concentration, which is in turn controlled by the spot area where sufficient flux is delivered to produce evaporation. Any operational system should therefore seek to maximize the evaporative spot area within available laser power. For low-power systems, the spot size is necessarily small, providing limited absorption and low detection probability.

As the laser strikes the target, melting and evaporation occur, forming a molecular cloud of target material in front of the heated spot. Thermal radiation from the spot will pass through the molecular cloud, where rotational and vibrational absorption will occur. The unique aspect of the R-LEMA approach is the idea of ‘backlighting *absorption*’, in contrast to existing methods that rely on detecting energy that is *emitted* by the target material. A critical aspect of the theoretical models is prediction of the plume density in front of the heated spot. Plume density determines the amount of absorption, driving the discernibility of absorption lines by the spectrometer. The ability to characterize absorption lines is directly related to the ability of the system to perform molecular composition analysis. Theoretical predictions of plume density and concomitant absorption can be tested by a straightforward experiment. A sample is placed in a vacuum space, mounted on a lab jack. The vacuum space is situated within the beam line of a Fourier Transform Infrared (FTIR) spectrometer. A laser beam is directed at the sample, through an optical window in the ceiling of the vacuum space. As the sample is heated, and evaporation begins, the FTIR beam passes through the molecular plume, via IR windows in the vacuum space sidewalls.

A critical aspect of the theoretical models is prediction of the plume density in front of the heated spot. Plume density determines the amount of absorption, driving the discernibility of absorption lines by the spectrometer. The ability to characterize absorption lines is directly related to the ability of the system to perform molecular composition analysis. The plume density is predicted to diminish rapidly with distance away from the spot, with a significant proportion of absorption occurring within one spot radius distance in front of the sample.

The proposed experiment will be capable of testing both plume density, and density-driven spectrometric absorption. Plume density can be explored by moving the sample up and down using the lab jack. As the sample is moved vertically, the FTIR beam passes through a different position within the plume. Recording multiple spectra with the beam passing through different portions of the plume will allow estimate of relative plume density as a function of distance in front of the spot. Comparison of spectra with laser on and laser off will allow estimates of absolute plume density. Measurements of relative and absolute plume density profiles can then be compared with theoretical predictions, thereby providing a test of the plume density theory.

Absorption lines must be discernible at the spectrometer. The pattern of absorption lines is used to determine which molecules are present in the plume. The theoretical models make predictions about the discernibility of absorption lines, based on plume density. The proposed experiment will produce measurements of absolute plume density. At the same time, the FTIR will be recording spectral intensity over a range of infrared wavelengths. The predicted absorption can be compared to the measured absorption at sampled wavelengths, thereby providing a test of the absorption theory.

The laboratory model requires a sufficiently powerful laser, on the order of ~ 1 kW, so as to mimic remote detection in an operational scenario. The target material is contained in a vacuum chamber. An optical window into the vacuum chamber provides a path for the laser beam. An infrared window into the vacuum chamber provides a viewing port for the spectrometer, which is situated in close proximity to the laser, similar to an operational configuration. Custom optics are required for the both laser and spectrometer, chosen to be analogous to a baseline operational scenario.

The target will be housed in a vacuum system. Target pressures inside the chamber would be $\sim 10^{-5}$ Torr during background sampling, *i.e.*, prior to laser activation. Once the laser is turned on, evaporation from the target may raise pressure in the chamber slightly. The vacuum chamber provides mounting for the two optical systems (laser and spectrometer). A concept drawing showing the laser mount and target chamber is shown in Fig. 3.

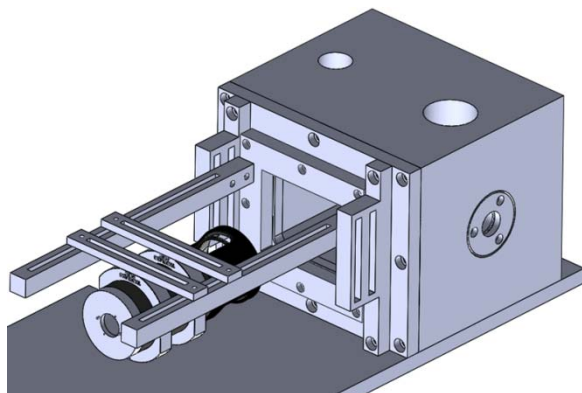


Figure 6-1: Concept for experimental setup. Laser and spectrometer optics are mounted outside the chamber, with visible and infrared windows through the

chamber wall.

The laser system will be based on laser fiber amplifier technology. A dual plano-convex lens system is used to focus the laser power onto the target through an optical window in the chamber wall, depicted in Fig. 4.

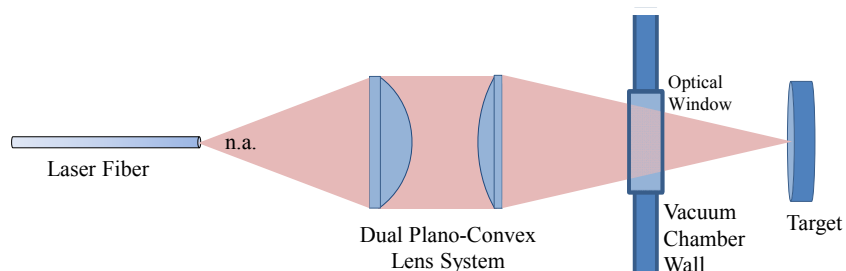


Figure 6-2: Concept for experimental setup. Laser and spectrometer are situated outside the vacuum chamber, which houses the target. Phase I results indicate that the bulk of absorption occurs within one spot radius of the target surface, so the path length inside the vacuum chamber can be short while still validating the basic concepts predicted by theory.

An infrared grating spectrometer is mounted outside the chamber, adjacent to the laser in a configuration that would be similar to a deployable system. A high spectral resolution instrument ($\sim 0.1 \text{ cm}^{-1}$) is required for discerning absorption lines and comparing with predicted spectra. Optics are required to focus on the signal emanating from the heated spot onto the spectrometer grating. In the laboratory setting, the heated spot will be on the order of $\sim 1 \text{ mm}$ radius on the surface of the target. Since spectrometer optics focus on the heated spot, the laboratory setup can be designed to mimic an operational scenario over much greater distances, by selecting an aperture that is analogous to any long-range situation.

Pure Materials for direct comparison to compounds studied in Phase I will be selected, so as to confirm the spectral absorption profiles. Pure materials will include minerals such as silica (SiO_2), titanium oxide (TiO_2) and water-bearing compounds. In addition to pure substances, rocky materials will be tested, including crustal rocks and minerals. Finally, asteroid regolith simulant will be tested, and attempts will be made to identify the simulant composition. Simulants of known composition will be analyzed, and compared with predicted spectra. Simulants with a blinded composition will also be analyzed, and composition determined experimentally will later be compared with the sealed simulant composition.

Raw spectra are acquired with the spectrometer software on a computer. Custom software will be developed to read and analyze the spectra, including implementation of background identification and subtraction algorithms. Many background and target spectra will be required for analysis, and storage and transmission schemes for operational scenarios will be explored.

In a typical FTIR implementation, a background spectrum is collected without the sample (Fig. 5). The sample is then placed in the beamline, and a sample spectrum is collected. The background is subtracted from the sample spectrum to produce a corrected sample spectrum. In the proposed R-LEMA method, no direct analog to a background spectrum is available. An alternative method includes positioning a heated blackbody in front of the spectrometer optics and recording as a spectrum that would serve as a background. Such a scheme would be compatible

with a deployable system. Algorithms would be required to adjust the effective temperature of the heated blackbody to match the temperature of the heated spot on the target.

Once background methods are established, spectra recorded from known and unknown samples will be compared to predicted spectra for pure materials. Composite materials, such as crustal rocks and asteroid regolith simulant, will be decomposed according to pure compound constituents algorithmically.

7. CONCLUSIONS

The system readiness of R-LEMA at the beginning of the NIAC Phase I research was TRL-1. NIAC Phase I research developed theoretical analysis of the underlying physical principles that support the system concept, elevating the system readiness to TRL-2. The analysis consists of theoretical models of sub-system operation, including laser optical propagation model, a target thermal model, estimation of evaporation of target material and resulting plume density, molecular absorption of radiation from the heated spot in the ejected plume, and estimation of the absorption lines that would be viewed by a spectrometer based on molecular cross sections of expected asteroid materials and absorption of thermal radiation in the ejected plume. Each sub-system model feeds into successive stages to provide an end-to-end model of the overall sensor system.

The feasibility of such a measurement depends on the details of the molecular cross section of the material in question and the laser power and distance to the target. Examples described in this paper indicate the possible sensitivity of this method for long range detection. The determination of the composition of asteroids and other targets supports several critical mission goals. The system concept could be elevated from TRL-2 to TRL-4, by building a proof-of-concept laboratory model and running extensive experiments to test the theory developed in Phase I. In particular, Phase I results suggests that the heated spot will produce sufficient blackbody flux to be viewed from a distance, so that flux is not the limiting component of the system. Phase I results also indicate that much of the absorption occurs within about one spot radius from the target. Thus, spectral detection is limited primarily by ejecta concentration, which is in turn controlled by the spot area where sufficient flux is delivered to produce evaporation. Any operational system should therefore seek to maximize the evaporative spot area within available laser power.

8. ACKNOWLEDGEMENTS

This research received financial support from the NASA Innovative Advanced Concepts (NIAC) Phase I program of the NASA Space Technology Mission Directorate (STMD). We would like to express our sincere gratitude for the truly outstanding support provided by the entire NIAC program staff, including Mr. Jason Derleth, Dr. Alvin Yew, Ms. Kathy Reilly and Dr. Ron Turner. Additionally, astute feedback from members of the NIAC External Council (NEC) was greatly appreciated, with special appreciation for discussions with NEC members Ms. Ariel Waldman, Dr. David Brin, and Dr. Louis D. Friedman. Support from several other NIAC fellows is also gratefully acknowledged, including Dr. Jim Mantovani and Dr. Robert Mueller (NASA Kennedy Space Center), Dr. Javid Bayandor (Virginia Polytechnic Institute and State University), and Dr. Siegfried Janson (The Aerospace Corporation). Finally, this research could not have come to fruition without substantial and selfless contributions from numerous researchers at UCSB and Cal Poly SLO. We wish to express our sincere gratitude to Dr. Prashant Srinivasan (Cal Poly),

Dr. Peter Meinhold (UCSB), and UCSB undergraduate students Jonathan Madajian, Alexander Cohen, Qicheng Zhang, Janelle Griswold, Dane Brouwer and Benton Miller.

9. REFERENCES

- A'Hearn, M.F., Belton, M.J.S., Delamere, W.A., Kissel, J., Klaasen, K.P., McFadden, L.A., Meech, K.J., Melosh, H.J., Schultz, P.H., Sunshine, J.M. and Thomas, P.C., 2005. Deep impact: excavating comet Tempel 1. *Science*, 310(5746), pp.258-264.
- Alvarez, L.W., Alvarez, W., Asaro, F. and Michel, H.V., 1979. Extraterrestrial cause for the Cretaceous-Tertiary extinction: Experimental Results and Theoretical Interpretation. *Science*, 208(4448), pp. 1095-1108.
- Balanis, C.A., 2016. *Antenna theory: analysis and design*. John Wiley & Sons.
- Barton, E. J., Yurchenko, S. N., and Tennyson, J., 2013. "ExoMol line lists–II. The Ro-Vibrational Spectrum of SiO," *Monthly Notices of the Royal Astronomical Society*, vol. 434(2), pp. 1469-1475.
- Berry, K., Suttery, B., Mayz, A., Williams, K., Barbee, B.W., Beckman, M., and Williams, B., 2013. OSIRIS-REx Touch-And-Go (TAG) mission design and analysis. In: *36th Annual AAS Guidance and Control Conference*, AAS 13-095.
- Brophy, J.R. and Muirhead, B., 2013. "Near-Earth Asteroid Retrieval Mission (ARM) Study," *Proc. of the 33rd International Electric Propulsion Conference*, IEPC-2013-082.
- Brownlee, D., Tsou, P., Aléon, J., Alexander, C.M.D., Araki, T., Bajt, S., Baratta, G.A., Bastien, R., Bland, P., Bleuet, P. and Borg, J., 2006. Comet 81P/Wild 2 under a microscope. *Science*, 314(5806), pp.1711-1716.
- Colombo, C., Vasile, M. and Radice, G., 2009. "Semi-Analytical Solution for the Optimal Low-Thrust Deflection of Near-Earth Objects." *Journal of Guidance, Control, and Dynamics*, 32(3), pp. 796-809.
- DeMeo, F.E., Binzel, R.P., Slivan, S.M. and Bus, S.J., 2009. An extension of the Bus asteroid taxonomy into the near-infrared. *Icarus*, 202(1), pp.160-180.
- Demtröder, W., 2013. *Laser Spectroscopy: Basic Concepts and Instrumentation*. New York: Springer Science & Business Media, 986 p., ISBN 978-3-662-05155-9.
- Gladman, B.J., Migliorini, F., Morbidelli, A., Zappala, V., Michel, P., Cellino, A., Froeschle, C., Levison, H.F., Bailey, M. and Duncan, M., 1997. Dynamical lifetimes of objects injected into asteroid belt resonances. *Science*, 277(5323), pp.197-201.
- Glassmeier, K.H., Boehnhardt, H., Koschny, D., Kührt, E. and Richter, I., 2007. The Rosetta mission: flying towards the origin of the solar system. *Space Science Reviews*, 128(1-4), pp.1-21.
- Glasstone, S., and Dolan, P., 1977. "The Effects of Nuclear Weapons, Third Edition," Washington: Department of Defense, ch. 2.
- Gibbings, M. A., Hopkins, J. M., Burns, D., & Vasile, M., 2011. "On Testing Laser Ablation Processes for Asteroid Deflection." 2011 IAA Planetary Defense Conference, Bucharest, Romania.
- Griswold, J., Madajian, J., Johansson, I., Pfau, K., Lubin, P., Hughes, G.B., Gilkes, A., Meinhold, P., Motta, C., Brashears, T. and Zhang, Q., 2015. "Simulations of directed energy thrust on rotating asteroids," *Nanophotonics and Macrophotonics for Space Environments IX*, edited by Edward W. Taylor, David A. Cardimona, Proc. of SPIE, v. 9616, pp. 961606-961606.
- Hansen, R.C., 2009. *Phased Array Antennas, Second Edition*, Wiley: New York.
- Harris, A.W. (1998), "A Thermal Model for Near-Earth Asteroids," *Icarus*, 131(2), 291-301.
- Hildebrand, A.R., Penfield, G.T., Kring, D.A., Pilkington, M., Camargo, A., Jacobsen, S.B. and Boynton, W.V., 1991. Chicxulub crater: a possible Cretaceous/Tertiary boundary impact crater on the Yucatán Peninsula, México. *Geology*, 19(9), pp.867-871.
- Hill, C., Yurchenko, S.N. and Tennyson, J., 2013. "Temperature-dependent molecular absorption cross sections for exoplanets and other atmospheres," *Icarus* vol. 226, pp. 1673-1677.

- Hughes, G.B., Lubin, P., Cohen, A., Madajian, J., Kulkarni, N., Zhang, Q., Griswold, J., and Brashears, T., 2016. "Remote laser evaporative molecular absorption spectroscopy," *Planetary Defense and Space Environment Applications*, edited by Gary B. Hughes, Proc. Of SPIE Vol. 9981, pp. 998119.
- Hughes, G.B., Lubin, P., Meinhold, P., O'Neill, H., Brashears, T., Zhang, Q., Griswold, J., Riley, J., and Motta, C., 2015. Stand-off molecular composition analysis. *Nanophotonics and Macrophotonics for Space Environments IX*, edited by Edward W. Taylor, David A. Cardimona, Proc. of SPIE Vol. 9616, pp. 961603.
- Jakhu, R. and Buzdugan, M., 2008. "Development of the natural resources of the moon and other celestial bodies: economic and legal aspects," *Astropolitics*, 6(3), pp.201-250.
- Klossek, P., Kullik, J. and van den Boogaart, K.G., 2016. "A systemic approach to the problems of the rare earth market," *Resources Policy*, vol. 50, pp.131-140.
- Kosmo, K., Pryor, M., Lubin, P., Hughes, G.B., O'Neill, H., Meinhold, P., Suen, J., C., Riley, J., Griswold, J., Cook, B.V., Johansson, I., Zhang, Q., Walsh, K., Melis, C., Kangas, M., Bible, J., Motta, C., Brashears, T., Mathew, S. and Bollag, J., 2014. "DE-STARLITE - a practical planetary defense mission," *Nanophotonics and Macrophotonics for Space Environments VIII*, edited by Edward W. Taylor, David A. Cardimona, Proc. of SPIE Vol. 9226.
- Lin, L.T., Archibald, D.D., and Honigs, D.E., 1988. Preliminary Studies of Laser-Induced Thermal Emission Spectroscopy of Condensed Phases. *Appl. Spectrosc.* 42(3), 477-483.
- Lisse, C.M., VanCleve, J., Adams, A.C., A'hearn, M.F., Fernández, Y.R., Farnham, T.L., Armus, L., Grillmair, C.J., Ingalls, J., Belton, M.J.S. and Groussin, O., 2006. Spitzer spectral observations of the Deep Impact ejecta. *Science*, 313(5787), pp.635-640.
- Lubin, P., Hughes, G.B., Eskenazi, M., Kosmo, K., Johansson, I., Griswold, J., Pryor, M., O'Neill, H., Meinhold, P., Suen, J., Riley, J., Zhang, Q., Walsh, K.J., Melis, C., Kangas, M., Motta, C. and Brashears, T., 2016. "Directed Energy Missions for Planetary Defense," *Advances in Space Research* 58(6), pp. 1093–1116.
- Lubin, P., Hughes, G.B., Bible, J. and Johansson, I., 2015. "Directed Energy for Planetary Defense and Exploration: Applications to Relativistic Propulsion and Interstellar Communications," *Journal of the British Interplanetary Society*, vol. 68, no. 5/6, pp. 172-182.
- Lubin, P. and Hughes, G.B., 2015. "Directed Energy for Planetary Defense." Chapter in: Allahdadi, Firooz, and Pelton, Joseph N. (Eds.), *Handbook of Cosmic Hazards and Planetary Defense*, Springer Reference, 1127 p., ISBN 978-3-319-03951-0.
- Lubin, P., Hughes, G.B., Bible, J., Bublitz, J., Arriola, J., Motta, C., Suen, J., Johansson, I., Riley, J., Sarvian, N., Clayton-Warwick, D., Wu, J., Milich, A., Oleson, M., Pryor, M., Krogen, P., Kangas, M., and O'Neill, H., 2014. "Toward Directed Energy Planetary Defense," *Optical Engineering*, 53(2), pp 025103-1 to 025103-18.
- Miziolek, A.W., Palleschi, V., and Schechter, I. (Eds.), 2006. *Laser Induced Breakdown Spectroscopy (LIBS): Fundamentals and Applications*. New York: Cambridge University Press, ISBN 978-0-521-85274-6.
- Morbidelli, A., 2005. Asteroid Population Models, Dynamics of Populations of Planetary Systems. *Proceedings IAU Colloquium No. 197*, Z. Knežević and A. Milani, eds.
- Müller, M.A., Schweizer, D. and Seiler, V., 2016. "Wealth effects of rare earth prices and China's rare earth elements policy," *Journal of Business Ethics*, vol. 138, pp. 627-648.
- Popova, O.P., Jenniskens, P., Emel'yanenko, V., Kartashova, A., Biryukov, E., Khaibrakhmanov, S., Shuvalov, V., Rybnov, Y., Dudorov, A., Grokhovsky, V.I. and Badyukov, D.D., 2013. Chelyabinsk airburst, damage assessment, meteorite recovery, and characterization. *Science*, 342(6162), pp.1069-1073.
- Rabinovich, V., and Alexandrov, N., 2013. "Typical Array Geometries and Basic Beam Steering Methods." In *Antenna Arrays and Automotive Applications* (pp. 23-54). Springer: New York.
- Riley, J., Lubin, P., Hughes, G.B., O'Neill, H., Meinhold, P., Suen, J., Bible, J., Johansson, I., Griswold, J. and Cook, B., 2014. "Directed energy active illumination for near-Earth object detection," *Nanophotonics and Macrophotonics for Space Environments VIII*, edited by Edward W. Taylor, David A. Cardimona, Proc. of SPIE Vol. 9226.
- Rothman, L.S., Gordon, I.E., Babikov, Y., Barbe, A., Benner, D.C., Bernath, P.F., Birk, M., Bizzocchi, L., Boudon, V., Brown, L.R. Campargue, A., Chance, K., Cohen, E.A., Coudert, L.H., Devi, V.M., Drouin, B.J., Fayt, A., Flaud, J.-M., Gamache, R.R., Harrison, J.J., Hartmann, J.-M., Hill, C., Hodges, J.T., Jacquemart, D., Jolly, A.,

- Lamouroux, J., Le Roy, R.J., Li, G., Long, D.A., Lyulin, O.M., Mackie, C.J., Massie, S.T., Mikhailenko, S., Müller, H.S.P., Naumenko, O.V., Nikitin, A.V., Orphal, J., Perevalov, V., Perrin, A., Polovtseva, E.R., Richard, C., Smith, M.A.H., Starikova, E., Sung, K., Tashkun, S., Tennyson, J., Toon, G.C., Tyuterev, V.I.G., and Wagner, G., 2013. “The HITRAN2012 molecular spectroscopic database,” *Journal of Quantitative Spectroscopy and Radiative Transfer*, vol. 130, pp. 4-50.
- Rothman, L.S., Gordon, I.E., Barber, R.J., Dothe, H., Gamache, R.R., Goldman, A., Perevalov, V.I., Tashkun, S.A. and Tennyson, J., 2010. “HITEMP, the high-temperature molecular spectroscopic database,” *Journal of Quantitative Spectroscopy and Radiative Transfer*, 111(15), pp.2139-2150.
- Sallé, B., Cremers, D.A., Maurice, S. and Wiens, R.C., 2005. Laser-induced breakdown spectroscopy for space exploration applications: Influence of the ambient pressure on the calibration curves prepared from soil and clay samples. *Spectrochimica Acta Part B: Atomic Spectroscopy*, 60(4), pp.479-490.
- Sallé, B., Lacour, J.L., Vors, E., Fichet, P., Maurice, S., Cremers, D.A. and Wiens, R.C., 2004. Laser-induced breakdown spectroscopy for Mars surface analysis: capabilities at stand-off distances and detection of chlorine and sulfur elements. *Spectrochimica Acta Part B: Atomic Spectroscopy*, 59(9), pp.1413-1422.
- Sanchez, J.P. and McInnes, C.R., 2012. “Assessment on the feasibility of future shepherding of asteroid resources,” *Acta Astronautica*, vol. 73, pp.49-66.
- Tennyson, J. and Yurchenko, S.N., 2012. “ExoMol: molecular line lists for exoplanet and other atmospheres,” *Monthly Notices of the Royal Astronomical Society* vol. 425, pp. 21-33.
- Vorontsov, M.A., Weyrauch, T., Beresnev, L.A., Carhart, G.W., Liu, L. and Aschenback, K., 2009. “Adaptive Array of Phase-Locked Fiber Collimators: Analysis and Experimental Demonstration,” *IEEE Journal of Selected Topics in Quantum Electronics*, vol. 15, 269.
- Walsh, K. J., Richardson, D. C. and Michel, P., 2012. “Spin-up of rubble-pile asteroids: Disruption, satellite formation, and equilibrium shapes,” *Icarus*, 220(2), 514-529.
- Yoshikawa, M., Fujiwara, A. and Kawaguchi, J.I., 2006. Hayabusa and its adventure around the tiny asteroid Itokawa. *Proceedings of the International Astronomical Union*, 2(14), pp.323-324.
- Zhang, Q., Walsh, K.J., Melis, C., Hughes, G.B. and Lubin, P.M., 2016. “Orbital Simulations on Deflecting Near Earth Objects by Directed Energy,” *Publications of the Astronomical Society of the Pacific*, 128(962), pp. 045001.
- Zhang, Q., Walsh, K.J., Melis, C., Hughes, G.B. and Lubin, P., 2015. “Orbital Simulations for Directed Energy Deflection of Near-Earth Asteroids”, in: Schonberg, W.P., Ed., Proceedings of the 2015 Hypervelocity Impact Symposium (HVIS 2015), *Procedia Engineering*, Vol. 103:671-678